

**Thesis title in english**

*Titre de la thèse en français*

**Thèse de doctorat de l'université Paris-Saclay**

École doctorale n°573 : INTERFACES - approches interdisciplinaires,  
fondements, applications et innovation  
Spécialité de doctorat : Sciences des matériaux  
Graduate School : Physique  
Référent : Faculté des sciences d'Orsay

Thèse préparée dans l'unité de recherche **Fondcombe**,  
sous la direction d'**Elrond**, seigneur de Fondcombe,  
et l'encadrement de **Gandalf**, magicien de l'ordre des Istari.

Thèse soutenue à Paris-Saclay, le 20 octobre 2028, par

**Hugo Lancery**

**Composition du jury**

Membres du jury avec voix délibérative

<b>Aragorn</b>	Président
Roi du Gondort	
<b>Legolas</b>	Rapporteur &
Prince des Elfes Sylvains	Examinateur
<b>Gimli</b>	Rapporteur &
Guerrier du royaume d'Erebore	Examinateur
<b>Faramir</b>	Examinateur
Intendant du Gondor	

**Titre :** Thesis title in english

**Mots-clés :** Or, montagne du Destin, Magie occulte

**Résumé :** Lorem ipsum dolor sit amet, consectetur adipiscing elit, sed do eiusmod tempor incididunt ut labore et dolore magna aliquam quaerat voluptatem. Ut enim aequo doleamus animo, cum corpore dolemus, fieri tamen permagna accessio potest, si aliquod aeternum et infinitum impendere malum nobis opinemur. Quod idem licet transferre in voluptatem, ut postea variari voluptas distingue possit, augeri amplificarique non possit. At etiam Athenis, ut e patre audiebam facete et urbane Stoicos iridente, statua est in quo a nobis philosophia defensa et collaudata est, cum id, quod maxime placeat, facere possimus, omnis voluptas assumenda est, omnis dolor repellendus. Temporibus autem quibusdam et aut officiis debitis aut rerum necessitatibus saepe eveniet, ut et voluptates repudiandae sint et molestiae non recusandae. Itaque earum rerum defuturum, quas natura non depravata desiderat. Et quem ad me accedit, saluto: 'chaere,' inquam, 'Tite!' lictores, turma omnis chorusque: 'chaere, Tite!' hinc hostis mi Albucius, hinc inimicus. Sed iure Mucius. Ego autem mirari satis non queo unde hoc sit tam insolens domesticarum rerum fastidium. Non est omnino hic docendi locus; sed ita prorsus existimo, neque eum Torquatum, qui hoc primus cognomen invenerit, aut torquem illum hosti detraxisse, ut aliquam ex eo est consecutus? – Laudem et caritatem, quae sunt vitae.

**Title :** Titre de la thèse en français

**Keywords :** Gold, Mount Doom, Occult magic

**Abstract :** Lorem ipsum dolor sit amet, consectetur adipiscing elit, sed do eiusmod tempor incididunt ut labore et dolore magna aliquam quaerat voluptatem. Ut enim aequo doleamus animo, cum corpore dolemus, fieri tamen permagna accessio potest, si aliquod aeternum et infinitum impendere malum nobis opinemur. Quod idem licet transferre in voluptatem, ut postea variari voluptas distingue possit, augeri amplificarique non possit. At etiam Athenis, ut e patre audiebam facete et urbane Stoicos iridente, statua est in quo a nobis philosophia defensa et collaudata est, cum id, quod maxime placeat, facere possimus, omnis voluptas assumenda est, omnis dolor repellendus. Temporibus autem quibusdam et aut officiis debitis aut rerum necessitatibus saepe eveniet, ut et voluptates repudiandae sint et molestiae non recusandae. Itaque earum rerum defuturum, quas natura non depravata desiderat. Et quem ad me accedit, saluto: 'chaere,' inquam, 'Tite!' lictores, turma omnis chorusque: 'chaere, Tite!' hinc hostis mi Albucius, hinc inimicus. Sed iure Mucius. Ego autem mirari satis non queo unde hoc sit tam insolens domesticarum rerum fastidium. Non est omnino hic docendi locus; sed ita prorsus existimo, neque eum Torquatum, qui hoc primus cognomen invenerit, aut torquem illum hosti detraxisse, ut aliquam ex eo est consecutus? – Laudem et caritatem, quae sunt vitae.

# Table of Contents

1	Optimal photometric geometries .....	5
1.1.	Remote sensing .....	5
1.2.	Mission context and objectives .....	5
1.2.1.	Generalities .....	5
1.2.2.	Moon's surface properties .....	6
1.2.3.	Objectives .....	6
1.2.4.	ESA Máni mission .....	6
1.3.	Creation of multiples orbital geometry .....	6
1.3.1.	Definition of the geometric parameters .....	6
1.3.2.	Stacked geometries .....	12
1.3.3.	Orbit precession .....	13
1.4.	Creation of multiple photometries .....	14
1.4.1.	Radiometric quantities .....	14
1.4.2.	Radiatif transfert .....	14
1.4.3.	Radiatif transfer analytic model .....	14
1.4.4.	Surface photometry .....	15
1.4.5.	Reflectance calculus .....	17
1.5.	Reflectance inversion to predict photometric parameters .....	17
1.5.1.	Differential Evolution of Markov Chain Monte Carlo algorithm .....	17
1.5.2.	Numerical implementation .....	18
1.5.3.	Inversion results .....	18
1.5.4.	Inversion efficiency .....	20
1.6.	Results .....	21
1.6.1.	Simulations, best orbits and noise level .....	21
1.7.	Comparision to Apollo 15 LRO mission .....	22
1.7.1.	Apollo LROC and Máni scenario design .....	22
1.7.2.	Comparison results .....	24
1.8.	Slope correction .....	26
2	Multifractal roughness .....	27
2.1.	Multifractal and cascade .....	27
2.2.	Multiscale analysis .....	28
2.2.1.	Haar fluctuations .....	29
2.3.	Multifractal generator .....	35
2.3.1.	Stable random variables generator .....	35
2.3.2.	FIF generator .....	36
2.4.	Synthetic topography modeling .....	36
2.4.1.	Deconvolution using Levy generator method .....	37
2.4.2.	Fourier filtering .....	39
2.4.3.	Formation UQ ed SMEMAG .....	40
3	Background .....	42
3.1.	What is Typst? .....	42
3.2.	Why a Typst Template? .....	42
4	Discussion .....	43
5	Conclusion .....	44
A	Appendix .....	47

# Introduction

This thesis serves as a tutorial and demonstration of the UniBasel Typst thesis template.

The template aims to simplify the thesis writing process by leveraging Typst's modern typesetting capabilities. Throughout this document, you'll find examples of citations, cross-references, mathematical formulas, figures, tables, and other essential elements commonly used in academic writing.

By the end of this tutorial, you should be familiar with all the template's features and be ready to write your own thesis using Typst.

# 1

## Optimal photometric geometries

### 1.1. Remote sensing

To enlight the reader on the remote sensing question treated in this chapter, the subject needs to be well introduced. When light reflects on a surface, what can we learn from its scattering properties and why it behaves in such a way.

### 1.2. Mission context and objectives



Figure 1: Schroter's Valley with meandering subrille, Mapping Camera Frame from Apollo 15 LRO<sup>1</sup> (A15-M-26II)  
(Credit: NASA)

#### 1.2.1. Generalities

The Moon is the only natural satellite of Earth and has a distance of 384,400 km from it. It also completes one orbital revolution in approximately 27.3 days, resulting in a synchronous rotation that keeps the same Moon's hemisphere facing Earth [1]. It has a mean radius of 1,737 km, the Moon is approximately 3.7 times smaller than Earth. The lunar body has an average density of  $3.34 \text{ g.cm}^{-3}$  and a gravity of  $1.62 \text{ m.s}^{-2}$ , which is almost 0.17 times what we can experience on Earth [2]. These fundamental characteristics directly influence lunar surface reflectance and photometric observations, observed from an observatory or space.

---

<sup>1</sup>Lunar Reconnaissance Orbiter

## 1.2.2. Moon's surface properties

The Moon's surface has many very distinct morphological characteristics that play a crucial role in photometry. These microtexture properties influence how light interacts with the surface, and perhaps are responsible for certain reflectance behaviour [3]. The lunar surface is characterized by two primary terrain types: the highlands, mostly composed of anorthositic rocks<sup>2</sup> with relatively high albedo, and the maria, extensive basaltic plains<sup>3</sup> with significantly lower albedo [4]. This great dichotomy in surface composition creates distinct photometric signatures that are even visible to the naked eye. In photometry, these properties are essential for modeling the interaction of light with the surface. One key parameter is the bidirectional reflectance distribution function BRDF<sup>4</sup>, which describes how light is reflected from the microtexture parameters, the illumination and viewing angles. The BRDF is critical for interpreting remote sensing data, mapping compositional variations, and understanding the geological history of the Moon. Accurate photometric analysis should also support exploration planning such as the ARTEMIS<sup>5</sup> mission and the identification of regions with potential ice deposits like the LCROSS<sup>6</sup> mission.

## 1.2.3. Objectives

The main goal of my work has been to compare and study different mission geometry. By looking at which geometry is the best one to characterize photometric properties, we aim to ensure the best scientific return of the mission. The conception of geometries with various emergence points of view, target positions and light incidences allow to simulate many different mission design and therefore see the full spectrum of possibility to find which one of them gives in output robust and reliable reflectance data. This evaluation is critical to improve the precision of future photometric models, advancing our understanding of the Moon's surface, and supporting future exploration missions.

## 1.2.4. ESA Máni mission

The Máni<sup>7</sup> mission is part of a recent program established by ESA<sup>8</sup> to support and provide access to space missions for smaller countries. This chapter of the thesis was developed during the mission's pre-phase A<sup>9</sup> stage, offering an opportunity for direct discussions and great returns from the scientific team on the mission requirements. The scientific ambition is to make the first lunar mission that combines great geometry diversity and high-resolution photometry. For this purpose the satellite will use a multiple-pass polar orbit strategy, flying at an altitude of 50 km. This orbital configuration is specially designed for high-resolution observations (20 cm/pix) and repeated measurements across a variety of lunar terrains. The satellite orbit has a precession of 1.03° and therefore a revisit period over the same target of 2 weeks. As a result, the estimated illumination angle shift at revisit is approximately 10°.

# 1.3. Creation of multiples orbital geometry

## 1.3.1. Definition of the geometric parameters

---

<sup>2</sup>Lunar anorthosites constitute the light-colored areas of the Moon's surface

<sup>3</sup>Lunar maria are plains of flood-basaltic lava flows that formed during the Moon's early volcanic history

<sup>4</sup>Bidirectional Reflectance Distribution Function

<sup>5</sup><https://www.nasa.gov/humans-in-space/artemis/>

<sup>6</sup><https://science.nasa.gov/mission/lcross/>

<sup>7</sup><https://activities.esa.int/4000146824>

<sup>8</sup>European Space Agency

<sup>9</sup>[https://www.esa.int/Science\\_Exploration/Space\\_Science/How\\_a\\_mission\\_is\\_chosen](https://www.esa.int/Science_Exploration/Space_Science/How_a_mission_is_chosen)

As previously mentioned with Màni, the satellite will conduct orbital revisits over the same target to gather photometric data with various geometry (incidence and emergence angles). For the sake of this section study, the Moon's surface was assumed as a perfect sphere, without slope. The left side of the Figure 2 explains the geometry through a global view. Here, the yellow star symbol (L, for light source) represents the sub-solar point of the Sun on the surface, while the green symbol (O, for observer) represents the observer point, which is the location of the satellite and the  $r^{\wedge}e$  symbol (T, for target) shows the target position. The right side of the image provides a more detailed, localized view of the target area on the Moon's surface, indicated by the point (T). Here, the orientation of the normal vector  $\vec{n}$  to the surface is highlighted, along with several critical angles that are essential to the photometric analysis.

- *The incidence:* ( $\theta_0$ ) angle ( $\vec{n} \wedge \vec{s}$ ) is the angle between the normal vector  $\vec{n}$  to the surface and the incoming sunlight.
- *The emergence:* ( $\theta$ ) angle ( $\vec{n} \wedge \vec{o}$ ) is the angle between  $\vec{n}$  and the line of sight from the satellite.
- *The phase:* ( $\alpha$ ) angle ( $\vec{n} \wedge \vec{o}$ ) is the angle between the direction of the incoming sunlight and the observer's line of sight.
- *The relative azimuth:* ( $\psi$ ) angle ( $\vec{n} \wedge \vec{o}$ ) angle defined the orientation of the satellite's view relative to the local coordinate frame on the surface.

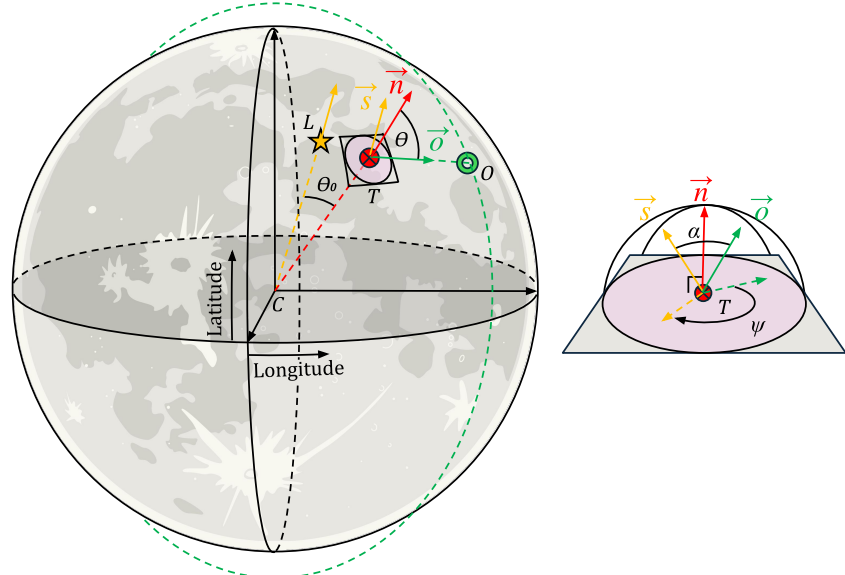


*Figure 2: Graph representing the system coordinates and geometries used for a given scenario, the left figure represents the global configuration view with the incidence, emergence angles and the Target in red, Light in yellow and Observer in green. The right figure represents a zoom on the normal plan from the target normal vector  $\vec{n}$  with the azimuth and phase angle. link*

We created many geometries with diversified Targets across the equator, medium, and high latitudes and illumination angles to evaluate later its impact on the inversion of the reflectance to predict photometric parameters. Therefore, to cover all possibility we made the following 15 geometries dataset.

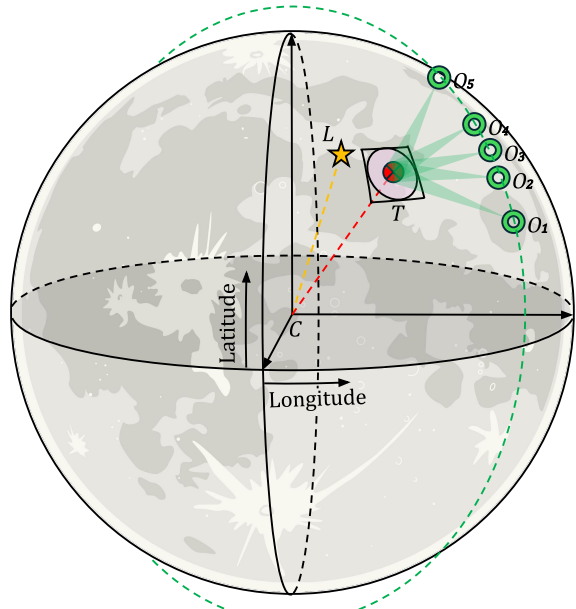


*Figure 3: Graph representing the satellite observations on its orbit passing over the target with a maximum emergence of  $80^\circ$ . In total 5 shots are taken, 2 from the maximum emergence angles close to  $80^\circ$  above and under the target latitude, 1 at nadir and 2 at an equal distance from the nadir and maximum emergence angle shot.* [link](#)

The Figure 3 showcase how we constraint the emergence angle. the satellite has a polar orbit at longitude  $0^\circ$  going from  $-180^\circ$  to  $180^\circ$  of latitude and we only retains 5 observations for a target within the emergence range of  $80^\circ$ . In total 5 shots are taken, 2 from the maximum emergence angles close to  $80^\circ$  above and under the target latitude, 1 at nadir and 2 at an equal distance from the nadir and maximum emergence angle shot. For this scenario, the subsolar point  $L$  in yellow, was placed at a high longitude on the equator, to simulate the illumination coming from forward. To make it more concise for the lecturer, the following Figure 4, Figure 5, Figure 6, Figure 7 and Figure 8 each represents 3 geometries that has a similar illumination and emergence angle but with different Target points  $T$  in red, magenta and purple that are spread out on the equator, medium, and high latitude respectively. They represents  $3 \times 5$  different geometries, later called E1, M1, H1 and E2, M2, H2 etc.

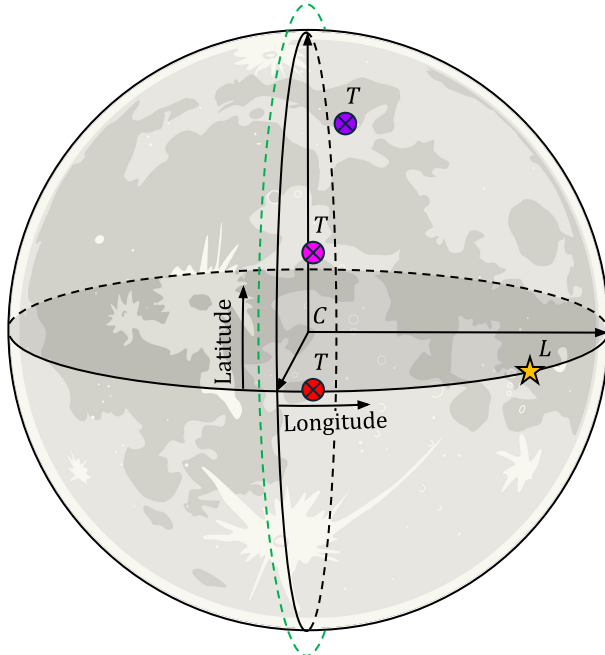


*Figure 4: Graph representing 3 different mission geometry E1, M1 and H1 with Targets respectively at ( $0^{\circ}\text{N}, 5^{\circ}\text{E}$ ), ( $45^{\circ}\text{N}, 5^{\circ}\text{E}$ ) and ( $70^{\circ}\text{N}, 10^{\circ}\text{E}$ ) with an illumination coming from forward. The Observer orbit is supposed fixed at  $0^{\circ}$  of longitude, allowing the Target longitude to act has the emergence angle variation (which greatly simplify the simulation).*

[link](#)

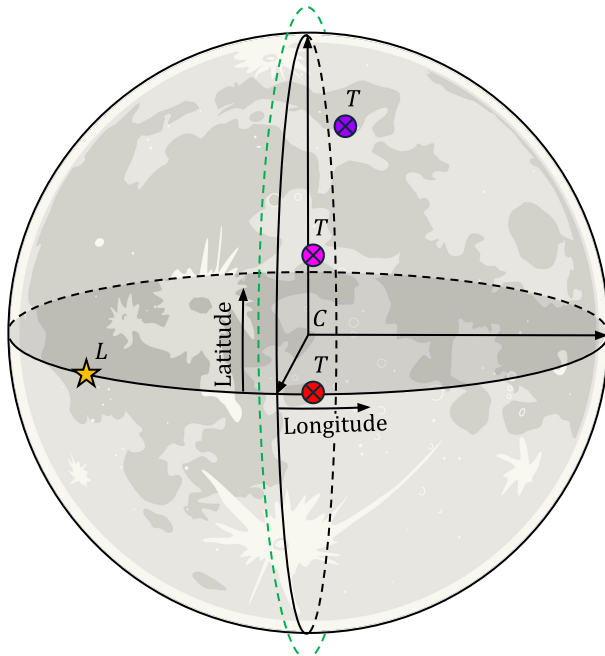


*Figure 5: Graph representing 3 different mission geometry E2, M2 and H2 with Targets respectively at ( $0^{\circ}\text{N}, 5^{\circ}\text{E}$ ), ( $45^{\circ}\text{N}, 5^{\circ}\text{E}$ ) and ( $70^{\circ}\text{N}, 10^{\circ}\text{E}$ ) with an illumination coming from backward. The Observer orbit is supposed fixed at  $0^{\circ}$  of longitude, allowing the Target longitude to act has the emergence angle variation (which greatly simplify the simulation).*

[link](#)

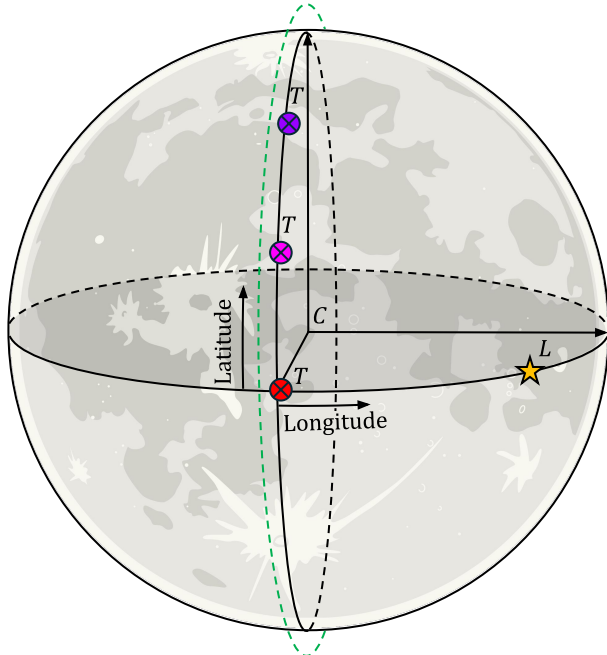


Figure 6: Graph representing 3 different mission geometry E3, M3 and H3 with Targets respectively at ( $0^{\circ}\text{N}, 0^{\circ}\text{E}$ ), ( $45^{\circ}\text{N}, 0^{\circ}\text{E}$ ) and ( $70^{\circ}\text{N}, 0^{\circ}\text{E}$ ) with an illumination coming from forward. The Observer orbit is supposed fixed at  $0^{\circ}$  of longitude, allowing the Target longitude to act has the emergence angle variation (which greatly simplify the simulation). [link](#)

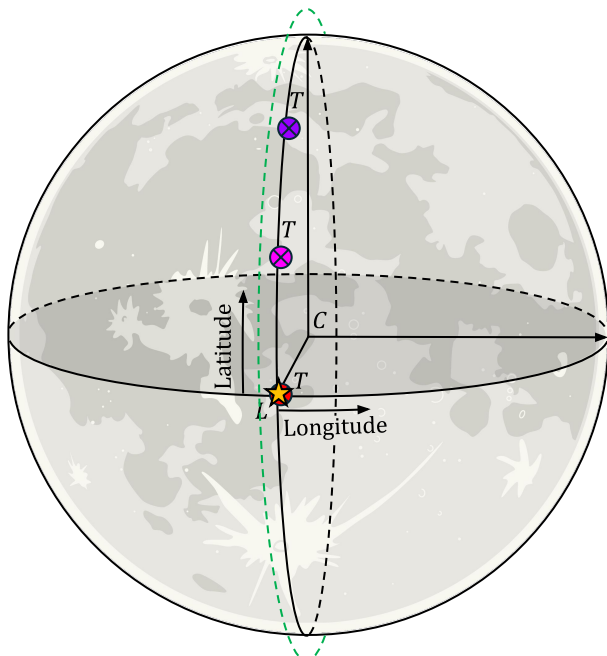
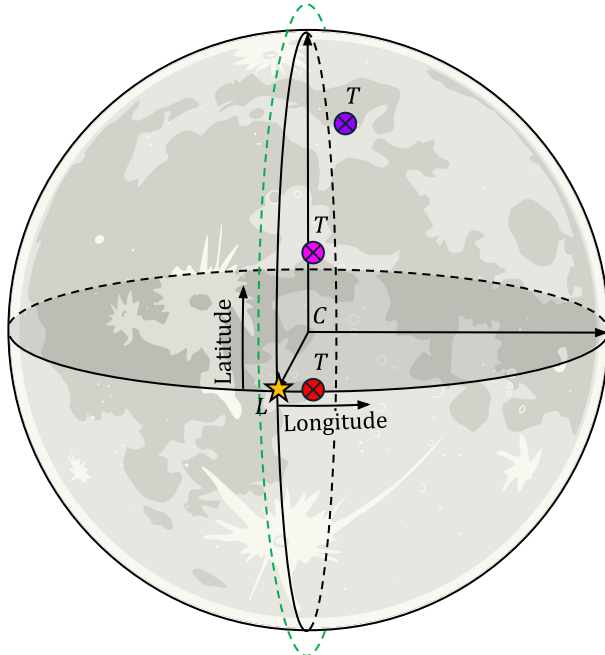


Figure 7: Graph representing 3 different mission geometry E4, M4 and H4 with Targets respectively at ( $0^{\circ}\text{N}, 0^{\circ}\text{E}$ ), ( $45^{\circ}\text{N}, 0^{\circ}\text{E}$ ) and ( $70^{\circ}\text{N}, 0^{\circ}\text{E}$ ) with an illumination coming from nadir. The Observer orbit is supposed fixed at  $0^{\circ}$  of longitude, allowing the Target longitude to act has the emergence angle variation (which greatly simplify the simulation). [link](#)



*Figure 8: Graph representing 3 different mission geometry E5, M5 and H5 with Targets respectively at (0°N, 5°E), (45°N, 5°E) and (70°N, 10°E) with an illumination coming from nadir. The Observer orbit is supposed fixed at 0° of longitude, allowing the Target longitude to act has the emergence angle variation (which greatly simplify the simulation).*

[link](#)

The Table 1 lists all the geometries made with 2 observers points of view (from nadir and on the side) and 3 different illuminations (from the left, nadir and right) across 3 different targets latitudes (at the equator, mid and high-latitude).

Coordinate (lon°, lat°)		
Target	Subsolar	Name
(5, 0)	(70, 0)	E1
(5, 0)	(-70, 0)	E2
(0, 0)	(70, 0)	E3
(0, 0)	(0.01, 0)	E4
(5, 0)	(0, 0)	E5
(5, 45)	(70, 0)	M1
(5, 45)	(-70, 0)	M2
(0, 45)	(70, 0)	M3
(0, 45)	(0.01, 0)	M4
(5, 45)	(0, 0)	M5
(10, 70)	(70, 0)	H1
(10, 70)	(-70, 0)	H2
(0, 70)	(70, 0)	H3
(0, 70)	(0.01, 0)	H4
(10, 70)	(0, 0)	H5

Table 1: Summary of all configurations used to analyze photometric responses across different latitudes, points of view and illuminations.

The objective is to cover a wide range of emergence and incidence angles through the geometry design to insure great reflectance inversion, since great geometry diversity helps to better understand photometry [5]. The Figure 9 showcases a target with different illumination angle and therefore different reflectances.

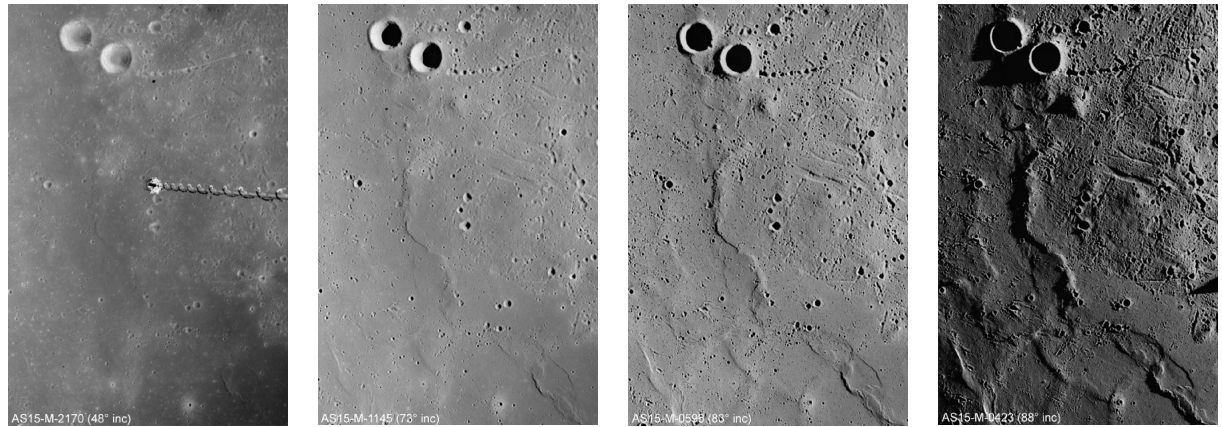


Figure 9: Four Apollo Metric frames of the same area in Mare Imbrium each taken under different solar illumination conditions. (AS15-M-2170 containing a robotic arm, AS15-M-1145, AS15-M-0598, and AS15-M-0423) (Credit: NASA)

### 1.3.2. Stacked geometries

A total of 93 geometries combinations were created, with a target at nadir, medium and high latitudes ( $0^\circ, 45^\circ, 70^\circ$ ) with different orbits relative longitudes ( $-10^\circ, 0^\circ, 10^\circ$ ). For each target position case (E, M and H) we stacked geometries up to 5 orbit type. For instance scenario E1, E1-E2, E1-E2-E3, but also all of them E1-E2-E3-E4-E5. This design simulate the satellite pass-by over the target each period or

more, with of course different geometry angles each time. For the sake of the computational time, the study was limited to 5 geometries with very distinct properties. There is in total 31 possible combinations possible. Obviously, it is not possible to combine geometries from target at equator and mid-latitude. Therefore, we are left with 93 total scenarios of combinations possible. We also used later in Section 1.7. 15 geometries from the Apollo 15 mission, observed by LRO. This set will be called ALRO and will be used to compare Màni design strategy with the actual Apollo 15 LRO camera.

### 1.3.3. Orbit precession

The purpose of this section is to verify the orbit precession of  $1.03^\circ$  to avoid any special case where we could have the same geometries at revisit. The mission goal is to generate as many different illumination and emergence angles, to create a wide variety of data. By default the illumination angle shifts at every orbital period, it can be calculated from the Moon's synodic period and the target revisit at nadir period of 29.53 and 27.43 days respectively, Equation 1. The RAAN<sup>10</sup> precession rate also needs to be considered, since it is a major perturbation Equation 2. It can be calculated from  $J_2$  and basic orbital parameters,  $R$ ,  $e$  and  $i$  and then added to the subsolar angle shift to approximate the total sun shift per revisit, Equation 3.

$$\Delta\theta_s = \left( \frac{360}{3600 \times 24} \times \left( \frac{T}{P_s \cdot \Delta\Omega} \right) - 1 \right) \times 360^\circ = -0.0733 \quad [\text{deg} \cdot T^{-1}] \quad (1)$$

$$\dot{\chi}\Omega = -\left(\frac{3}{2}\right)J_2\left(\frac{R^2}{a^2(1-e^2)^2}\right)n\cos(i)\left(\frac{180^\circ}{\pi}\right) \cdot T = -0.0108 \quad [\text{deg} \cdot T^{-1}] \quad (2)$$

$$\Delta\theta_t \approx \Delta\theta_s + \dot{\chi}\Omega = -0.0841 \quad [\text{deg} \cdot T^{-1}] \quad (3)$$

The following Figure 10 describes how the illumination angle changes at each revisit (per period of revisit  $T$ ). It clearly demonstrates how well the design is defined, with an illumination shift of 2 local hours per revisits.

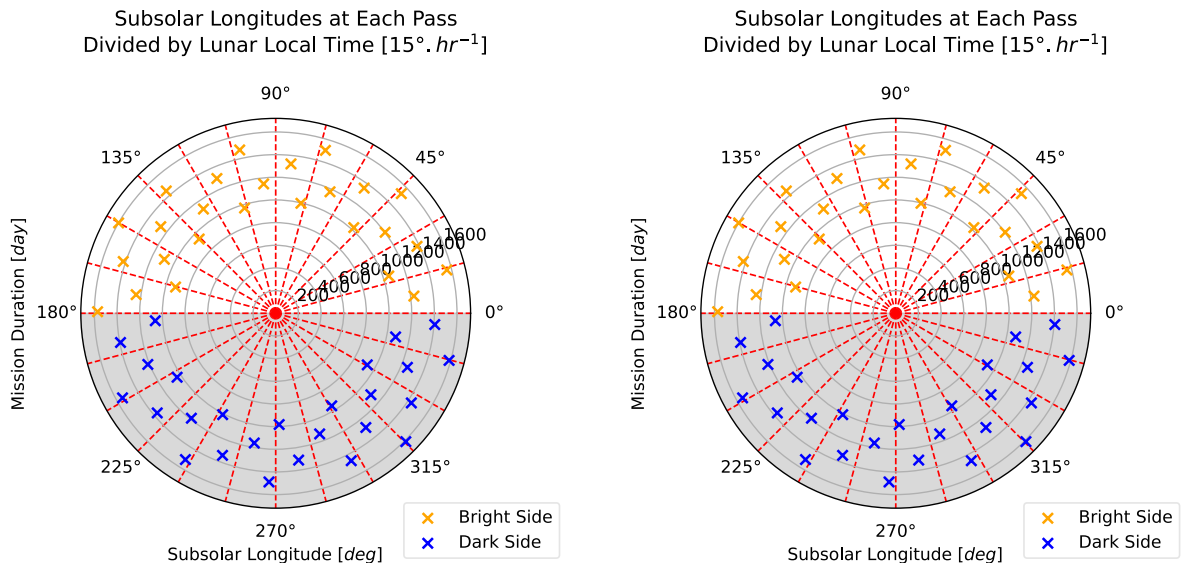


Figure 10: The left polar plot shows the illumination angle variation at each revisit during 2 years, while the right polar plot shows the sun local hour on the moon shifting at each revisits during 2 years. [link](#)

<sup>10</sup>Right Ascension of the Ascending Node

## 1.4. Creation of multiple photometries

### 1.4.1. Radiometric quantities

This are physical quantities used to measure electromagnetic radiation (including light), based on its energy. Examples include:

- *Radiant flux*: ( $\Phi$ ) [ $J.s^{-1}$ ] the total power of radiation is the energy quantity received or emitted by a surface per unit of time in all directions.
- *Irradiance*: ( $E$ ) [ $W.m^{-2}$ ] power of radiation per unit area,  $E = \frac{d}{\Phi} dS$ .
- *Radiant intensity*: ( $I$ ) [ $W.sr^{-1}$ ] power per unit solid angle.
- *Radiance*: ( $L$ ) [ $W.m^{-2}.sr^{-1}$ ] the irradiance per unit solid angle,  $L = \frac{IE}{\pi F \cos(\theta_0)}$ .

From those quantities can be defined the reflectance function, therefore in this study the Bidirectional Reflectance Distribution Function also called BRDF was used. It satisfies several key properties :

- Helmholtz reciprocity principle : Let  $(\theta_0)$  and  $(\theta)$  be respectively the directions of incidence and emergence, therefore  $r(\theta_0, \theta) = r(\theta, \theta_0)$ .
- Energy conservation principle : The radiant flux ( $\Phi$ ) reflected by the surface over the entire hemisphere is less than or equal to the incident flux

### 1.4.2. Radiatif transfert

As described by [3], it is convenient to define a quantity called the albedo factor ( $\gamma$ ) of the medium as well as the incidence cosinus ( $\mu_0$ ) and the emergence cosinus ( $\mu$ ) :

$$\gamma = \sqrt{1 - \omega}, \quad \mu_0 = \cos(\theta_0), \quad \mu = \cos(\theta) \quad (4)$$

[6] proposed an equation to describe radiative transfer, describing the energy loss and gain as electromagnetic radiation passes through a plane-parallel layer of a material. This material is optically inactive, meaning it has no internal sources. It continuously scatters and absorbs radiation, and is illuminated from above by a flux  $F$ . The radiance  $L_e$  emerging from this same layer is described by the photon transport equation. This equation shows that energy is conserved within the layer. Changes in radiance in a given direction happen either because energy is absorbed or scattered away (extinction), or because radiation comes in from other directions (scattering), including directly from the source. The local energy balance of the radiation field at a point, per unit normal surface area and per unit solid angle, between two levels  $\tau$  and  $\tau + d\tau$ , is written as follows Equation 4 .

$$\mu \frac{\delta L_{e(\tau, \mu, \psi)}}{\delta \tau} = L_{e(\tau, \mu, \psi)} - \frac{F}{4\pi} \exp\left(\frac{-\tau}{\mu_0}\right) P(g) - \frac{1}{4\pi} \int_{-1}^1 \int_0^{2\pi} \omega P(g) L_e(\tau', \mu', \psi') d\mu' d\psi' \quad (5)$$

The Equation 5 is composed of the extinction, the simple diffusion and multiple diffusion functions, respectively corresponding to the first, second and last term.

### 1.4.3. Radiatif transfer analytic model

The expression of the semi-empirical Hapke model corresponding to the 1993 version is presented in this section. The analytic model is derived from the radiative transfer Equation 5, while addressing the limitations of the far-field approximation, which does not apply well to dense granular media. First, the base model assumes that light interacts with the average local properties of scattering and absorption within the volume, rather than with the exact spatial distribution of individual structures. It begins by

modeling the interaction between an incoming light beam and a single isolated particle, using the single-scattering albedo ( $\omega$ ) and the phase function ( $\Phi$ ). Multiple scattering ( $H$ ) is then treated separately. Next, the model takes into account the surface effects caused by the close packing of particles. This includes the opposition effect ( $B$ ), surface roughness ( $\zeta$ ), and the suppression of diffraction in the single scattering term.

$$\text{Ref}(\theta_0, \theta, \alpha) = \frac{\omega}{4\pi} \frac{\mu_0}{\mu_0 + \mu} ([1 + B(\alpha)]P(\alpha) + H(\mu_0)H(\mu) - 1) \quad [\text{sr}^{-1}] \quad (6)$$

In radiative transfer, the Chandrasekhar function ( $H$ ) describes the angular distribution of the reflected rays from a medium. It is critical for modeling multiple scattering-light that bounces more than once within a particulate surface such as regolith for our case. In it's approach [3], Hapke uses a simplified version of Chandrasekhar's radiative transfer theory.

$$H(x) = \left( 1 - [1 - \gamma]x \left[ r_0 + \left( 1 - \frac{r_0}{2} - r_0 x \right) \ln \left( \frac{1+x}{x} \right) \right] \right)^{-1} \quad (7)$$

The single-particle phase function ( $p$ ) represents how light is scattered by a single particle as a function of the phase angle ( $\alpha$ ).

$$P(\alpha) = \frac{(1-c)(1-b^2)}{(1+2b\cos(\alpha)+b^2)^{1.5}} + \frac{c(1-b^2)}{(1-2b\cos(\alpha)+b^2)^{1.5}} \quad (8)$$

The Equation 9 is the Hapke shadow-hiding opposition effect function. It's designed to model the non-linear brightening of a surface when the phase angle approach zero. At small phase angles, the shadows cast by a surface are hidden from the observer's view. As a results, more of the surface appears fully illuminated, making the surface look brighter than expected from standard scattering alone.

$$B(\alpha) = \frac{B_0}{1 + (\frac{1}{h}) \tan(\frac{\alpha}{2})} \quad (9)$$

#### 1.4.4. Surface photometry

For the surface photometry we assume to follow the Hapke model [3] described in Equation 6. For the target surface, we set a variety of 12 photometry types using different parameters listed in Table 2. Perhaps, we have :

- *The single scattering albedo:* ( $\omega$ ) represents the fraction of incident light scattered by a single particle rather than absorbed, providing insight into the material's reflectivity, with values ranging from 0 (completely absorbing) to 1 (completely scattering).
- *The Hapke mean slope roughness:* ( $\zeta$ ) quantifies the macroscopic roughness of a surface influencing light scattering and shadowing effects.
- *The opposition effect amplitude:* ( $B_0$ ) describes the magnitude of the sharp brightness.
- *The asymmetry:* ( $b$ ) characterizes the angular distribution of scattered light, distinguishing isotropic ( $b = 0$ ), forward-scattering ( $b > 0$ ), and back-scattering ( $b < 0$ ) behaviors.
- *The back-scattering fraction:* ( $c$ ) defines the proportion of light scattered back toward the source, with higher values indicating surfaces with irregular or opaque particles.
- *The opposition effect width:* ( $h$ ) represents how sharply the brightness increases near zero phase angle.

Different photometry types also means different microtextures simulated. Therefore the light interaction changes depending on these parameters, for example with high asymmetry ( $b$ ) and low back-scattering

(c) tends to characterize smooth and clear microtexture. While low asymmetry (b) and high backscattering (c) tends to characterize internal scattered grain microtexture, as shown in Figure 11.

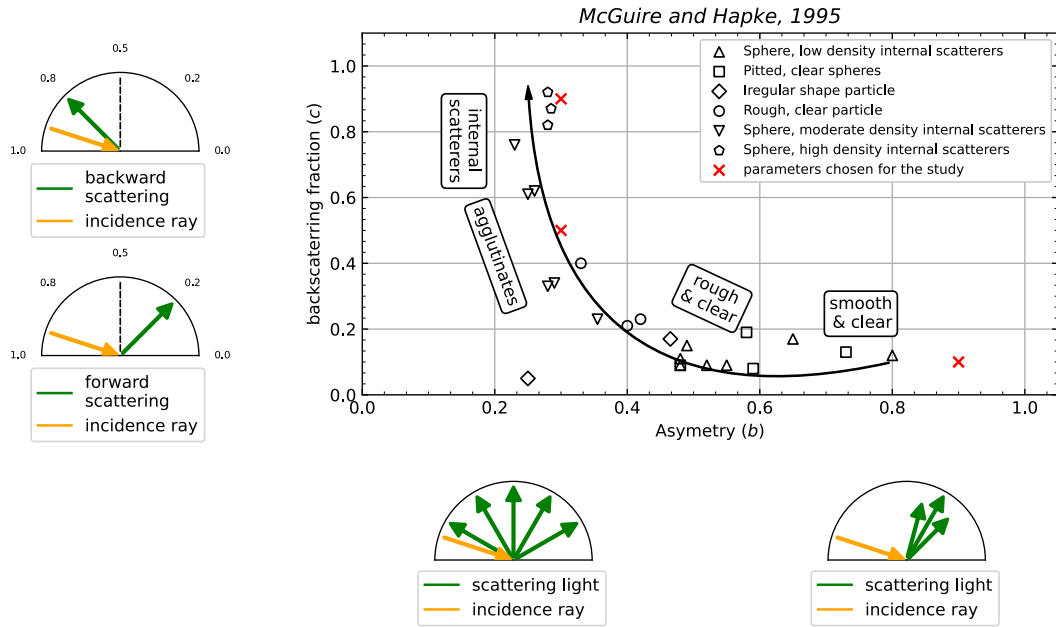


Figure 11: Particle phase function parameter results from experimental studies on artificial [7] and natural samples [8] having varied physical properties, resulting in different photometric behaviours. link

In Table 2 encompasses all the possible photometric behaviour on the lunar surface [9] as described in Section 1.2.2.. The parameters  $b_0$  and  $h$  are due to the opposition effect and easily constrained at low phase angle [5]. For this particular reason, it was removed from our study and set to a constant (0.5).

$\omega$	$b$ & $c$	$\zeta$	$B_0$	$h$
0.3	(0.3,0.9)	0	0.5	0.5
0.9	(0.3,0.9)	0	0.5	0.5
0.3	(0.3,0.5)	0	0.5	0.5
0.3	(0.9,0.1)	0	0.5	0.5
0.9	(0.3,0.5)	0	0.5	0.5
0.9	(0.9,0.1)	0	0.5	0.5
0.3	(0.3,0.9)	30	0.5	0.5
0.9	(0.3,0.9)	30	0.5	0.5
0.3	(0.3,0.5)	30	0.5	0.5
0.3	(0.9,0.1)	30	0.5	0.5
0.9	(0.3,0.5)	30	0.5	0.5
0.9	(0.9,0.1)	30	0.5	0.5

Table 2: Summary of all configurations used to analyze photometric responses across different latitudes, points of view and illuminations.

By evaluating these scenarios, we aim to better understand how reflectance behaves under different microtexture conditions, informing the optimal choice of parameters for the mission's orbital configurations.

#### 1.4.5. Reflectance calculus

The bidirectional reflectance is calculated for all photometric set of parameters Table 2 and geometric orbit combinations Table 1. It has in inputs the photometric parameters, incidence, emergence, phase and azimuth angles, see Equation 6. The calculus is based on Hapke's photometric model [3] previously described and goes through the surface roughness corrections, shadowing effects, multiple scattering effect within particles, the opposition effect and phase function dependence. This part of the study has for objective to simulate the reflectance received by the satellite, which we will then inverse using the geometric orbit angles to approximate photometric parameters and conclude whether or not the scenario is well suited to approximate the surface photometric parameters. The synthetic reflectance was then combined with a measured tolerance of 10%, 5% and 2% later referred as ( $\sigma$ ) to simulate realist measurement.

### 1.5. Reflectance inversion to predict photometric parameters

#### 1.5.1. Differential Evolution of Markov Chain Monte Carlo algorithm

To retrieve the photometric parameters of a planetary surface, we use the Hapke model described in the previous section as our forward model. This model simulates how light reflects off a dense granular surface based on physical parameters. However, estimating these parameters from reflectance measurements is an inverse problem, which we approach using a Bayesian python framework. The aims is to generate samples from a target probability distribution ( $\pi$ ) of the Hapke BRDF input parameters, in our case a posterior distribution in Bayesian inference, described by Equation 13. For that, we have the likelihood function  $\mathcal{L}(\theta) = P(D|\theta)$  which tells how likely the observed data (D) is, based on a set of initial parameters ( $\theta$ ). Also their is the prior, which is the initial belief about the parameters before seeing any data is set to a Gaussian distribution centered at zero:

$$p(\theta_i) = \mathcal{N}(0, \sigma_i^2) \quad (10)$$

The evidence (also called the normalizing constant) is:

$$P(D) = \mathcal{L}(D|\theta) \cdot p(\theta) d\theta \quad (11)$$

In our study and using the mc3 tool we assume independent Gaussian errors on the data points. This leads to the likelihood function, Equation 12:

$$\mathcal{L}(\theta) \propto \exp\left(-\frac{1}{2} \sum_n^{i=1} \left(\frac{y_i - f(x_i, \theta)}{\sigma_i}\right)^2\right) \quad (12)$$

Where  $y_i$  are the observed data points,  $f(x_i, \theta)$  is the prediction model with  $x_i$  representing the geometry and  $\theta$  the photometric parameters, and  $\sigma_i$  are the uncertainties for each data point. This expression is equivalent to minimizing the chi-square statistic.

$$\pi(\theta | D) = \frac{\mathcal{L}(D|\theta) \cdot p(\theta)}{P(D)} \quad (13)$$

A Markov Chain is constructed in a way that its stationary distribution is  $\pi(\theta)$ . At each step, with a given state  $t$ , given the current state  $\theta^{\{(t)\}}$ , a candidate  $\theta^*$  is proposed from a proposal distribution  $\sim q(.|\theta^{\{(t)\}})$  and through the Equation 14} it is then accepted or rejected (probability).

$$\eta = \min \left( 1, \frac{\pi(\theta^*) \cdot q(\theta^{(t)} | \theta^*)}{\pi(\theta^{(t)}) \cdot q(\theta^* | \theta^{(t)})} \right) \quad (14)$$

In the DE-MCMC<sup>11</sup> method, multiple independent chains are initiated and evolve in parallel. At each iteration, a candidate for a chain is proposed by combining two other chains, as described in Equation 15.

$$x^* = x^{(a)} + \gamma(x^{(b)} - x^{(c)}) + \varepsilon \quad (15)$$

Here ( $\gamma$ ) is a scaling factor and ( $\varepsilon$ ) is a gaussian noise. This method enhances a better sampling efficiency in high-dimensional problems by combining multiple chains and dynamically adapting step sizes.

### 1.5.2. Numerical implementation

The inversion can be calculated with the Python MC3 (Multi-Core Markov Chain Monte Carlo) library. It is a powerful Python tool for Bayesian parameter estimation and model fitting, with great details on the statistic output. It uses the MCMC method to sample the posterior probability distribution of the function parameters. It has features like adaptive step-size tuning and Gibbs sampling [10] to ensure that the parameter space is thoroughly explored. MC3 provides detailed results, including posterior distributions, parameter uncertainties, and convergence quality, making it a valuable tool for a statistical analysis.

For this study, the sample function from the MC3 library was used, requiring in entry the reflectance measured and it's uncertainties, the reflectance calculus function from the Section 1.4.5. with it's accompanying arguments and finally the initialization parameters for the algorithm in it self. The sample function returns very interesting results such as, the best parameters fit, the thinned posterior distribution, the  $X^2$  values for the posterior samples, the mean of the marginal posteriors for each model parameter and the standard deviation of the marginal posteriors for each model parameter.

### 1.5.3. Inversion results

Figure 12 showcases the given results from the inversion method. To evaluate the quality of the inversion algorithm over the true parameters, we refined the thinned posterior distribution by excluding the burn-in phase and filtering out unwanted data, ensuring that the goodness-of-fit metric between the model and the observed data was limited to values less than 30. This allow to get only the final converged results that can be quantified and estimated, later used in Section 1.5.4.. The following Figure 12 represents all the reflectance posterior distribution over the phase for all shots of the scenario, here we have the combination of the orbit H1, H2, H3, H4, and H5 for  $\omega = 0.3$ ,  $b = 0.3$ ,  $c = 0.9$ ,  $\zeta = 30$ ,  $o = 0.5$ ,  $h = 0.5$ , with 5 shots per orbit.

---

<sup>11</sup>Differential Evolution Markov Chain Monte Carlo

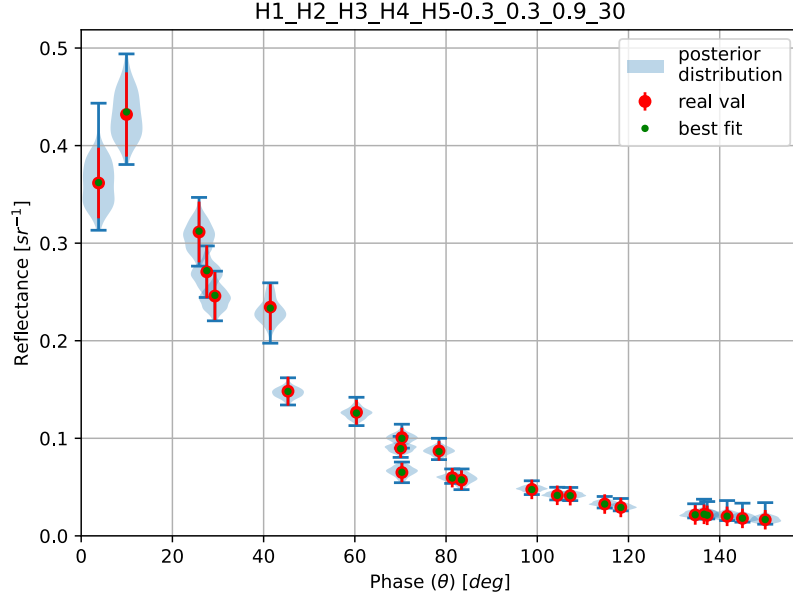


*Figure 12: Example of the fit distribution results with 25 images geometry from the combination of the orbit H1, H2, H3, H4, and H5 (5 images per orbit) for a surface photometry set by  $\omega = 0.9$ ,  $b = 0.3$ ,  $c = 0.9$ ,  $\zeta = 30$ ,  $b_0 = 0.5$ ,  $h = 0.5$ . The  $10^5$  sample solutions are in black. The true solution is in red with an uncertainty of  $\sigma = 10\%$ . The maximum likelihood is in green. The sample solution distribution, plotted in light blue, is close to the expected synthetic observation in red.*

The typical computation time for a run is 1 minute for 100 000 samples and the data produce is around 27 Mb on a 6 cores multi-thread laptop machine. This has been run more than 1116 time to produce the following results. For each orbit type (E, M and H) and for each different noise level (10%, 5% and 2%). The following figure represents the thinned posterior distribution, without the burn-in phase delimited where the chisq output is  $> 30$ . It greatly exhibits co-relation between photometric parameters, indeed it is a great tool to quickly see if a combination of geometry and photometry works well together.

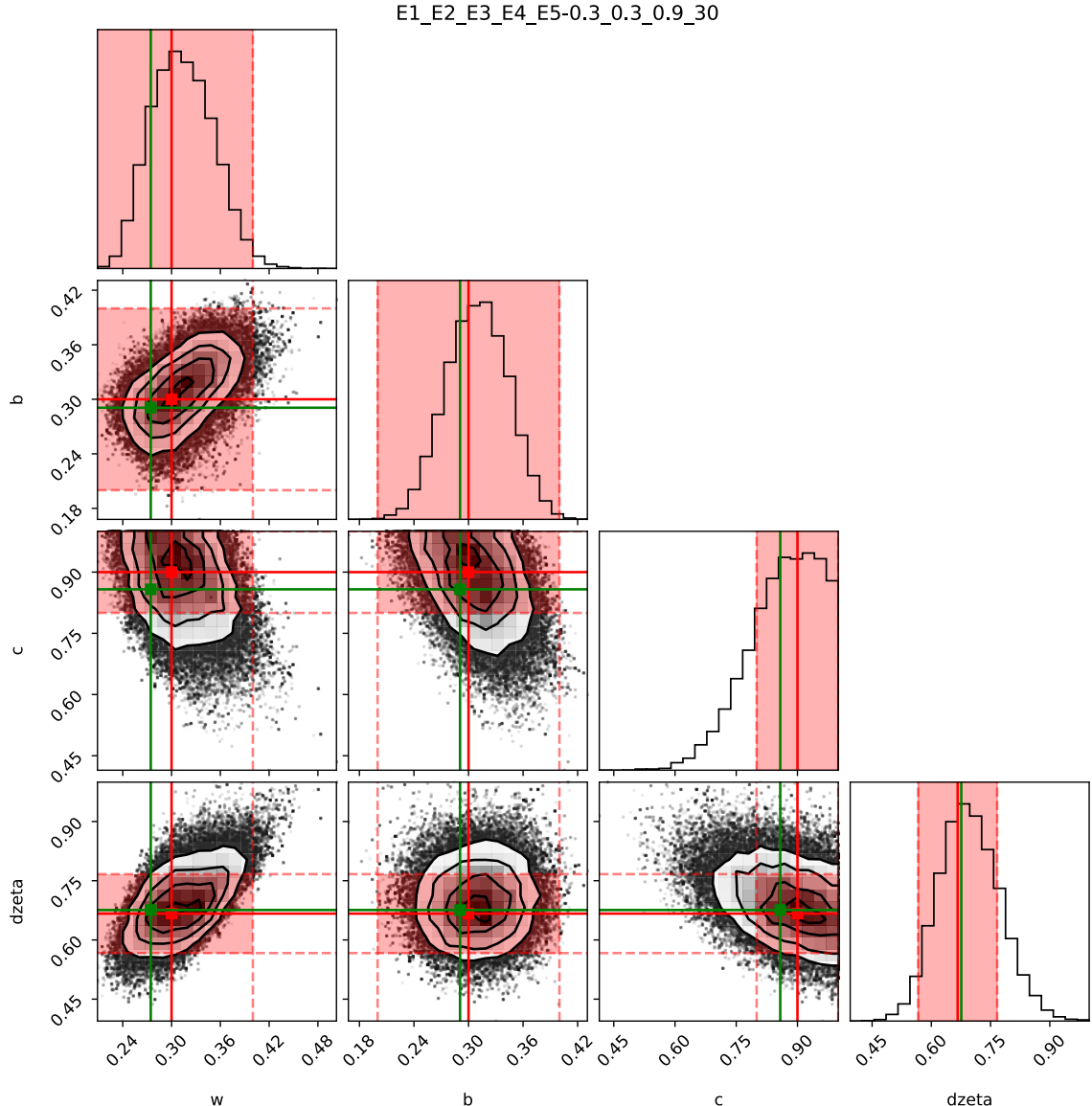


*Figure 13: Example of the fit distribution results with 25 images geometry from the combination of the orbit E1, E2, E3, E4, and E5 (5 images per orbit) for a surface photometry set by  $\omega = 0.3$ ,  $b = 0.3$ ,  $c = 0.9$ ,  $\zeta = 30$ ,  $b_0 = 0.5$ ,  $h = 0.5$ . The  $10^5$  sample solutions are in black. The true solution is in red with an uncertainty of  $\sigma = 10\%$  and the lightred area represents the acceptable range ( $\varepsilon \pm 10\%$ ) used to quantify the inversion quality (see Section 1.5.4.).*

#### 1.5.4. Inversion efficiency

To simulate a mission, we combined all the geometries and photometries to make a single data set of 1116 different scenarios. We evaluate each scenario by using the efficiency  $E$  and the strategy defined in [5].

- Synthetic reflectance calculus : The reflectance corresponding to each of the 1116 different scenarios (all combinations of possible 93 geometry and 12 photometry) are computed.
- From synthetic reflectance to photometric parameters : For each of the 1116 scenario, the Bayesian inversion is performed, incorporating noise/uncertainty level (encompassing all uncertainties on the absolute reflectance level of the image) of  $\sigma = 10\%$ ,  $5\%$  and  $2\%$ .

- Synthesis of the results : The quality of the geometric set is determined by the knowledge on the photometric parameters. This is estimated by the efficiency  $E$ , that is averaged among all 12 photometry.

The closer the solution to the true parameter set is, the better the estimate. We measure the quality of the tested geometry by considering, for every parameter (for example the true parameter  $\omega'$ ), the part of the distribution  $\sigma(\omega')$  which lies inside the interval  $[\sigma(\omega') - \varepsilon, \sigma(\omega') + \varepsilon]$ , where  $\varepsilon$  is set to 10% which is relevant for a lunar science case. Let us denote  $I_\omega = \int_{\omega' - \varepsilon}^{\omega' + \varepsilon} \sigma(\omega) d\omega$ . In practice,  $I_\omega$  is simply estimated by considering the proportion of samples  $\omega_\ell$  that fall inside the correct interval among the  $N_{\text{samp}}$  samples that were drawn. We then consider:

$$D_\omega = -\log(I_\omega) \quad (16)$$

$D_\omega$  decreases with  $I_\omega$ , equals 0 when the full distribution  $\sigma(\omega)$  falls inside the correct interval. The total efficiency distance  $E$  of a given geometry is finally defined by the sum:

$$E = D_\omega + D_b + D_c + D_{\bar{\theta}} \quad (17)$$

To convert back this proxy to a probability, we just have to evaluate  $e^{-E}$  that is the probability of the distribution that stands within the acceptable margin. The lowest the proxy  $E$ , the better constraint are the photometric parameters. We can define a threshold given the uncertainties, 50% of the posterior distribution should stand within an acceptable range.

This lead to a maximum value of  $E = -\log(0.5) = 0.69$ .

## 1.6. Results

### 1.6.1. Simulations, best orbits and noise level

We are left with the following results from the efficiency of each scenario, characterizing the quality of the geometric configuration for the inversion of a particular surface photometry. Results are presented for each orbit type (E, M, H) and for each noise level ( $\sigma$ ) values. (For full results, see Table 10}).

Target at Equator with $\varepsilon = 10\%$						
Nb.	$\sigma = 10\%$		$\sigma = 5\%$		$\sigma = 2\%$	
Shots	Geometry	Proxy E	Geometry	Proxy E	Geometry	Proxy E
5	E2	3.5817	E2	3.2158	E2	2.5636
10	E2-3	1.7769	E2-3	1.0902	E2-3	0.4468
15	E1-2-4	0.7900	E1-2-4	0.3546	E1-2-3	0.1122
20	E1-2-3-4	0.6717	E1-2-3-5	0.2845	E1-2-3-4	0.0876
25	all	0.6079	all	0.2648	all	0.0852

Table 3: Best geometry combination per number for all photometry at Equator; with the proxy of acceptable range set to  $\varepsilon = 10\%$

Target at Mid latitude with $\varepsilon = 10\%$						
Nb.	$\sigma = 10\%$		$\sigma = 5\%$		$\sigma = 2\%$	
Shots	Geometry	Proxy E	Geometry	Proxy E	Geometry	Proxy E
5	M3	3.7549	M2	2.1260	M4	1.0458
10	M1-2	1.7009	M2-4	0.5603	M2-4	0.1001
15	M1-2-4	1.0113	M1-2-4	0.2866	M1-2-4	0.0385
20	M1-2-3-4	0.7207	M1-2-3-4	0.2252	M1-2-3-4	0.0262
25	all	0.6623	all	0.2072	all	0.0257

Table 4: Best geometry combination per number for all photometry at Medium latitudes, with the proxy of acceptable range set to  $\varepsilon = 10\%$

Target at High latitude with $\varepsilon = 10\%$						
Nb.	$\sigma = 10\%$		$\sigma = 5\%$		$\sigma = 2\%$	
Shots	Geometry	Proxy E	Geometry	Proxy E	Geometry	Proxy E
5	H4	1.7607	H4	0.9829	H4	0.5242
10	H2-4	0.6372	H2-4	0.1644	H2-4	0.0119
15	H1-2-4	0.4137	H1-2-4	0.0790	H2-3-4	0.0009
20	H1-2-3-4	0.3089	H1-2-3-4	0.0505	H1-2-3-4	0.0003
25	all	0.2667	all	0.0410	all	0.0003

Table 5: Best geometry combination per number for all photometry at High latitudes, with the proxy of acceptable range set to  $\varepsilon = 10\%$

As expected, the inversion results are better for a lower noise level  $\sigma = 10\%$  than for a higher noise level  $\sigma = 2\%$ . From Table 3, Table 4 and Table 5 we can see that a combination of 5 orbits at  $\sigma = 10\%$  is equivalent to a single orbit combination at  $\sigma = 2\%$ . This behavior is consistent across all orbit types and photometric models, and implies that a higher SNR<sup>12</sup> is greatly beneficial for the inversion process. We can also observe an improvement in the inversion results for very bad cases, in deed the worst results at low noise level is equivalent to the best one at high level (See Table 10). We can therefore deduce the importance of the SNR regarding the quality of inversions.

## 1.7. Comparision to Apollo 15 LRO mission

In this section the objectif is to argument the impact of our design over the same target and number of observations compared to the LROC<sup>13</sup>.

### 1.7.1. Apollo LROC and Mani scenario design

To recreate both datasets, the Target was set to a latitude of  $26^\circ$ . The “ALRO” for Apollo LRO dataset is composed of 15 images took by the LROC with their emergence, incidence, north-incidence azimuth and north-emergence azimuth during it’s mission (see Table 6). The Apollo Mani design in return is

<sup>12</sup>Noise Signal Ratio

<sup>13</sup>Lunar Reconnaissance Orbiter Camera

composed of 5 different geometries (see Table 7) and a similar Target set to  $26^\circ$  of latitude which were combined as described in Section 1.3.2..

$\psi_i$	$\theta_0$	$\psi_e$	$\theta$
93.7513	81.5486	347.5870	0.2638
96.6906	77.3477	181.6242	0.7427
108.3253	59.6203	196.2753	0.4608
116.3151	49.3139	358.8516	0.1476
131.4637	38.6037	101.9953	0.3460
179.5545	27.6331	243.7643	0.1635
204.5473	30.0536	352.8963	0.1689
229.3753	35.2895	150.3110	0.3939
227.2929	37.3696	78.1265	0.1346
250.6272	56.8386	84.4090	0.8264
253.1356	58.1126	313.5851	0.6215
264.9080	79.1644	96.6980	1.0920
265.3669	80.0679	139.6722	0.1343
265.8143	80.9764	261.3323	0.9213
266.3602	82.8294	269.2535	0.1736

Table 6: Apollo LROC 15 observations geometry angles, with  $\psi_i$  the notrth-incidence azimuth,  $\theta_0$  the incidence,  $\psi_e$  the north-emergence azimuth and  $\theta$  the emergence.

Coordinates			
	Target	Subsolar	Name
Observer ↑ -180	(5, 26)	(70, 0)	A1
	(5, 26)	(-70, 0)	A2
	(0, 26)	(70, 0)	A3
	(0, 26)	(0.01, 0)	A4
	(5, 26)	(0, 0)	A5

Table 7: Summary of all configurations used to analyze photometric responses, points of view and illuminations (See Table 1).

The Figure 14 displays the new angle ( $\psi_i$ ) and ( $\psi_e$ ) from Apollo data, used to retreive  $\vec{s}$  and  $\vec{o}$  (respectively the Target → Light and the Target → Observer vecotrs).  $R_{\vec{v}}(\theta)$  represents the rotation of a vector around axis  $\vec{v}$  of an angle  $\theta$ . From this representation and the data from Table 6}, we calculated back the subsolar and emergence vectors through Equation 18} and Equation 19}, which are essential for the code pipeline and the Hapke reflectance model.

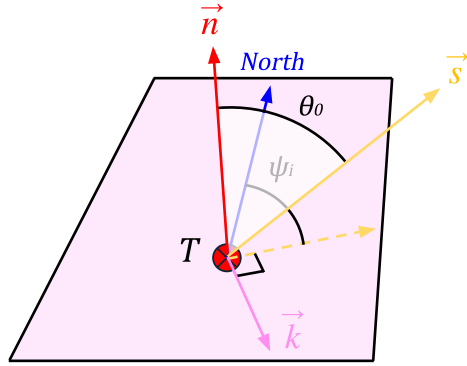


Figure 14: Representation of the normal plan from the target normal vector  $\vec{n}$  with the incidence ( $\theta_0$ ) and incidence-north azimuth ( $\psi_i$ ). This figure clarify how the ALRO data where converted in order to use the code pipeline and the inversion. (link to the drawing)

$$\text{proj}_{\vec{n}_\perp}(\vec{s}) = R_{\vec{n}}(\psi_i) \times \vec{N} \quad (18)$$

$$\vec{s} = R_{\vec{k}}(\theta_0) \times \vec{k} \quad (19)$$

### 1.7.2. Comparison results

Table 8 represents the efficiency  $E$  for different scenarios. For a realistic lunar microtexture, Máni is better than LRO, even with 1 single orbit (5 images of orbit A1) versus 15 images of LROC. Given our science goal of a maximum value of  $E = 0.69$ , the optimum Máni scenario is with 3 orbits A1+A2+A4 at 10% noise/uncertainty level and 2 orbits A2+A4 at 5% noise & uncertainty level (corresponding to  $2 \times 2$  pixels binning).

As an illustration of these results, Figure 15 to Figure 16 presents the results for the most typical lunar photometry. In each of these figures, on left the Máni scenario is presented in comparison with the actual LROC data. Figure 15 presents 2 Máni orbits at 10% noise/uncertainty level. Figure 15 presents 2 Máni orbits at 5% noise/uncertainty level (corresponding to  $2 \times 2$  pixels binning).

Figure 16 presents 3 Máni orbits at 10% noise/uncertainty level. For all those cases, the improvement of Máni is clear in comparison to the LROC. This is due to the relative small range in phase and emergence angle in the LROC observation strategy.

In addition, Máni can achieve very high phase angle (larger than  $90^\circ$ ) which is required to fully constrain the photometric parameters, as also noticed in cite{2015\_Schmidt\_ICA}. To illustrate this point, the previous photometric inversion proposed on LROC data was ASSUMING the roughness  $\zeta$  cite{2014\_Sato\_JGRP}. With Máni, we will be able to actually constrain it.

Nb. / Shots	Target at 26° of latitude with $\varepsilon = 10\%$					
	$\sigma = 10\%$		$\sigma = 5\%$		$\sigma = 2\%$	
	Geometry	Proxy E	Geometry	Proxy E	Geometry	Proxy E
15	ALRO	4.8204	ALRO	3.9648	ALRO	2.8113
5	A1	3.6571	A2	3.0491	A4	1.7451
10	A2-4	1.5995	A2-4	0.7816	A1-2	0.2071
15	A1-2-4	0.8335	A1-2-4	0.3158	A1-2-3	0.0808
20	A1-2-3-4	0.7227	A1-2-3-4	0.2660	A1-2-3-4	0.0654
25	all	0.6399	all	0.2432	all	0.0598

Table 8: Best geometry combination per number for all photometry at 26° of latitude, with the proxy of acceptable range set to  $\varepsilon = 10\%$

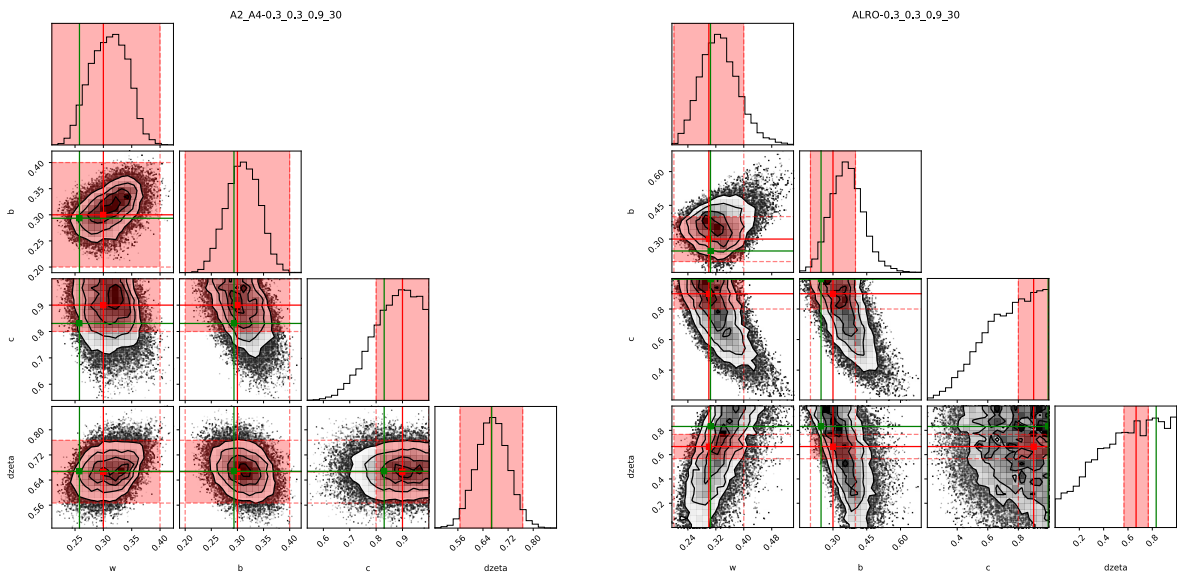
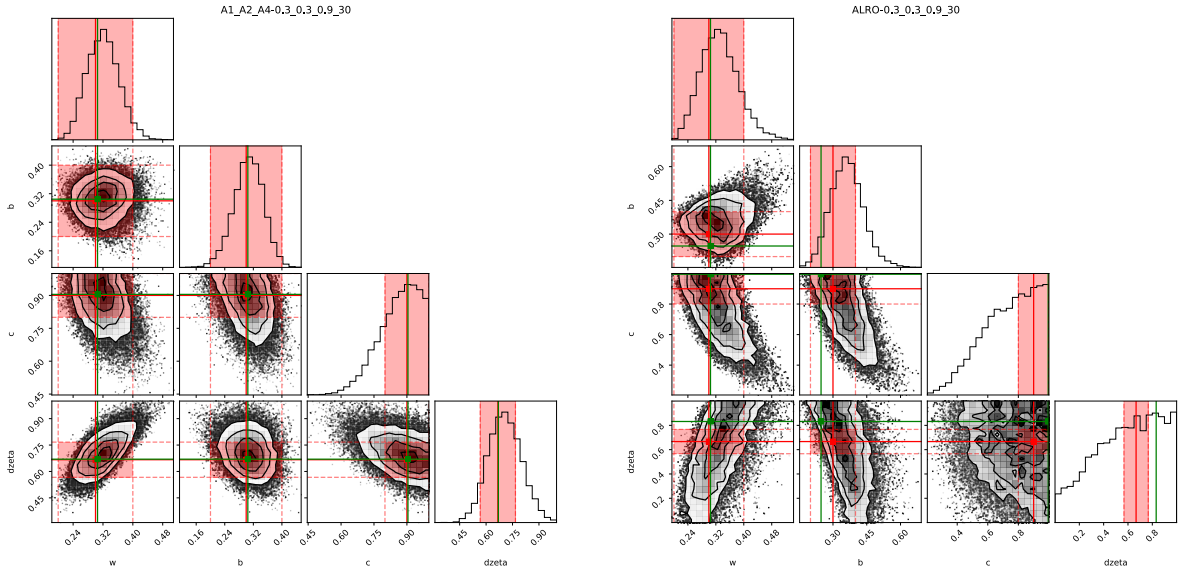


Figure 15: Inversion distribution results for the Apollo 15 target. The photometry is set to typical lunar surface  $\omega = 0.3$ ,  $b = 0.3$ ,  $c = 0.9$ ,  $\zeta = 30$ ,  $o = 0.5$ ,  $h = 0.5$ . Noise/uncertainty level is set to 5% for Máni and 10% for ALRO. Due to the uncertainties on all available data, the black distribution, representing the solution's state of information, is spread around the true value. The  $\varepsilon = 10\%$  acceptable domain is in light red. The maximum of likelihood is in green. (left) for 2 Máni orbit, 10 images from orbit A2+A4. The proxy is  $E=1.16$  ( $e^{-1.16} = 31.2\%$  of the acceptable solutions are within 10% margin) (right) with the 15 images from LROC. The proxy  $E=2.73$ . ( $e^{-2.73} = 6.6\%$  of the acceptable solutions are within 10% margin). The improvement of Máni is clear in comparison to LROC. This is due to the relative small range in phase angle in the LROC observation strategy, that we surpass with Máni.



**Figure 16:** Inversion distribution results for the Apollo 15 target. The photometry is set to typical lunar surface  $\omega = 0.3$ ,  $b = 0.3$ ,  $c = 0.9$ ,  $\zeta = 30$ ,  $o = 0.5$ ,  $h = 0.5$ . Noise/uncertainty level is set to 10%. Due to the uncertainties on all available data, the black distribution, representing the solution's state of information, is spread around the true value. The  $\varepsilon = 10\%$  acceptable domain is in light red. The maximum of likelihood is in green. (left) for 3 Máni orbit, 15 images from orbit  $A1+A2+A4$ . The proxy is  $E=0.72$  ( $e^{-0.72} = 48.5\%$  of the acceptable solutions are within 10% margin). (right) with the 15 images from LROC. The proxy  $E=2.73$ . ( $e^{-2.73} = 6.6\%$  of the acceptable solutions are within 10% margin). The improvement of Máni is clear in comparison to LROC. This is due to the relative small range in phase angle in the LROC observation strategy, that we surpass with Máni.

## 1.8. Slope correction

The surface roughness can induce the emergence, incidence and azimuth angles to be rotated around the normal axis. This results in a wrong interpretation of the global mission geometry, particularly for our design where those parameters were supposed ideal without even taking in account other perturbations (e.g., crater steep sides, etc.). In this section, we tackle this problem to see its impact on the inversion results.

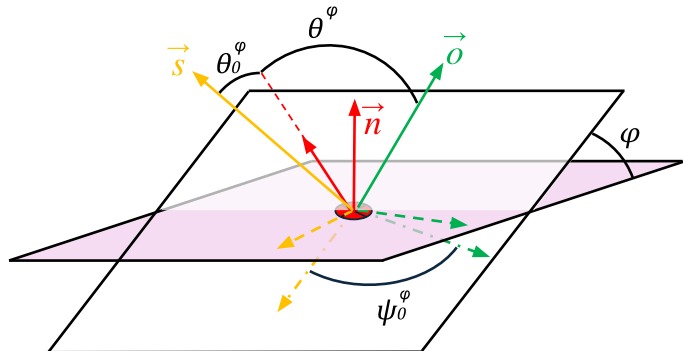


**Figure 17:** Representation of the inclined normal plan from the target normal vector  $\vec{n}$  with the incidence ( $\theta_0^\varphi$ ), emergence ( $\theta^\varphi$ ), azimuth ( $\psi_\varphi$ ) and the slope ( $\varphi$ ) angle. (link to the drawing)

# 2

## Multifractal roughness

### 2.1. Multifractal and cascade

The cascade phenomena is a quite simple process that can be underlying complex mechanism. Indeed, cascade are the core process of redondent and turbulent processes [11] such as cloud structures or surface topography. This cascade idea goes back to 1941 from Kolmogorov law [12] and for the  $\beta$ -model we will see in Section 2.4. to the Novikov-Stewart model [13]. Scaling or scale invariance data, made of a repeating pattern, are usually anaylised through multifractal tools. They offer a great way to describe behaviour that follows a law through different scale, of distance in our roughness case. Planetary topography is clearly turbulent across distance scale or/and time, fractals are a fantastic tool to characterize them such as quiescence volcanic plains to chaotics dead river's bed, see Figure 18.

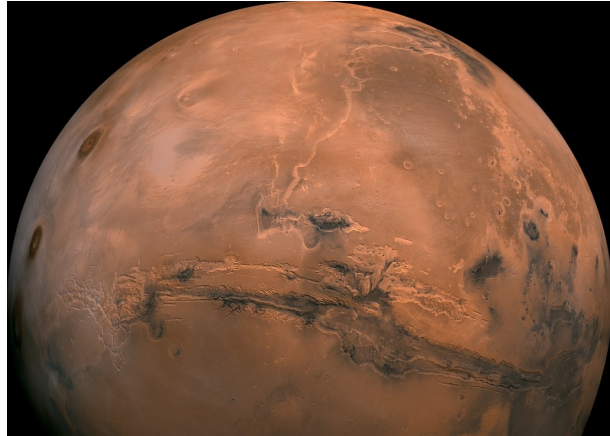


Figure 18: Mars view took by the Viking Orbiter. Mosaic of the Schiaparelli hemisphere of Mars projected into point perspective, a view similar to that which one would see from a spacecraft. The images were acquired in 1980 during early northern summer on Mars.

From a given signal  $f$  possessing self similar properties, its statistical variability can be studied across scales using structure functions. We first define the kind of variation we are interested in like Equation 21 or Equation 26, which will returns a scalar per specific conditions (at time  $t$ , scale  $\Delta x$ , etc.). For all those scalars results we are then interested to look for the global scalling property through different scales, which is what the structure function Equation 20 is used for.

The scale  $\Delta x$  is a subdivision value of the overall signal length  $L$  (outer scale), for the roughness this characteristic is a distance in meter or pixels. As we said, to statistically quantify how the signal varies across different scales, it is common to use a tool called structure function. This structure function of order  $q \in \mathbb{R}^+$  at scale  $\Delta x$  can be defined as

$$S_q(\Delta x) = \frac{1}{N} \sum_{x=1}^N |\delta_{\Delta x} f(x)|^q \quad (20)$$

where for example

$$\delta_{\Delta x} f(x) = f(x + \Delta x) - f(x) \quad (21)$$

In the structure function, the order  $q$  controls the sensitivity to variation. Indeed, small  $q$  emphasizes frequent and typical variations, while large  $q$  amplifies rare and extreme variations. Structure functions naturally follow a power-law scaling over a range of scales.

$$\begin{aligned} S_q(\Delta x) &\sim \langle \varphi_q(\Delta x) \rangle \Delta x^{qH} \\ \langle \varphi_q(\Delta x) \rangle &= \left( \frac{L}{\Delta x} \right)^{K(q)} \end{aligned} \quad (22)$$

Where the turbulent flux  $\varphi$  is a multifractal cascade,  $H$  represents the rate at which mean fluctuations grow ( $H > 0$ ) or decrease ( $H < 0$ ) with scale and  $K(q)$  the moment scaling function describing how the moment changes with scale. The final definition can be expressed as

$S_q(\Delta x) \sim \Delta x^{\xi(q)}, \quad \xi(q) = qH - K(q)$

(23)

In the simplest case,  $\delta_{\Delta x} f(x)$  is the increment. More generally, it can be replaced by multiresolution quantities such as wavelet coefficients in Section 2.2.1..  $N \approx \frac{n}{\Delta x}$  in Equation 20 is the number of fluctuations available at scale  $\Delta x$ , for a signal of total length  $n$ . In the classical quasi-Gaussian case, where  $K(q) = 0$ , makes  $\xi(q)$  linear, this regime is called monofractal. However, for the results of a multifractal regime,  $K(q)$  is generally non linear and convex and characterizes the intermittency. For example, in Kolmogorov's (1941) theory [12],  $f(x)$  is the velocity,  $\varphi$  is the energy flux  $\varepsilon^{\frac{1}{3}}$  and one obtains the scaling law  $\xi(q) = q \cdot \frac{1}{3}$ . Empirical multifractal analysis essentially consists of estimating the scaling  $\xi(q)$ . These scaling exponents are commonly involved in various data analysis tasks, such as detection, identification, or classification.

Over the last 30 years, structure functions based on differences and with concave rather than linear  $\xi(q)$  have been successfully applied to many geophysical processes (atmospheric [14] and geological [15] processes). It turns out that the use of differences to define the fluctuations is overly (and needlessly) restrictive. The need to define fluctuations more flexibly motivated the development of new wavelets [16] & [17], which are now the widely used. However for geological and surface study, the classical Haar fluctuation sometimes referred as the “poor man’s wavelet” since it reduces to simple differences, is indeed robust, easy to understand and sufficient for our purposes.

## 2.2. Multiscale analysis

Planetary geomorphism shine by its variety and uniqueness, from desertic teluric planets to gas giants. These Geological processes, at the core of planets surface and atmosphere origin, took place across huge time-space scales. To interpret the geometrical complexity of such phenomena, we consider  $\varphi$  the underlying turbulent flux of the topography. A widely used method is the Fourier analysis which outline the contribution of structures of a given frequency to the total variance of the process [14].

Before 1930, the main branch of mathematics leading to wavelets began with Joseph Fourier and his theories of frequency analysis. He asserted that any  $2\pi$ -periodic function  $f(x)$  is the sum

$$a_0 + \sum_{k=1}^{\infty} (a_k \cos(kx) + b_k \sin(kx)) \quad (24)$$

of its Fourier series. The coefficients  $a_0$ ,  $a_k$  and  $b_k$  are calculated by

$$a_0 = \frac{1}{2\pi} \int_0^{2\pi} f(x) dx, \quad a_k = \frac{1}{\pi} \int_0^{\infty} f(x) \cos(kx) dx, \quad b_k = \frac{1}{\pi} \int_0^{\infty} f(x) \sin(kx) dx \quad (25)$$

Fourier's assertion played an essential role in the evolution of the ideas mathematicians had about the functions. He opened up the door to a new functional universe.

Naturally some mathematicians began to shift from frequency analysis to the notion of scale analysis. That is, analyzing  $f(x)$  by creating mathematical structures that vary in scale see Equation 20. In our case, multiscale analysis were conducted through an elegant new way popularized by mandelbrot called fractals which also later led to multifractals.

The first mention of wavelets see Equation 26 (fluctuations function) appeared in an appendix to the thesis of A. Haar (1909) [18]. One property of the Haar wavelet is that it has compact support, which means that it vanishes outside of a finite interval. Unfortunately, Haar wavelets are not continuously differentiable which somewhat limits their applications. However, for clarity and simplicity, real-space analysis tools are preferable. In this section we aim at characterizing planets surfaces roughness properties for some reasons.

### 2.2.1. Haar fluctuations

A natural way to quantify fluctuations across scales is through increments, defined in Equation 21. While simple, this definition has practical limitations: it may be sensitive to noise, and it only captures differences between two points, without accounting for the average variability within the interval [19]. To address this, wavelet-based approaches have often been used. In particular, the Haar wavelet provides a simple and robust framework for analyzing fluctuations across scales. Its associated fluctuation function is denoted  $\mathcal{H}$ .

$$\mathcal{H}(\Delta x) = \frac{2}{\Delta x} (f(x) + f(x + \Delta x) - 2f(x + \frac{\Delta x}{2})) \quad (26)$$

where

$$f(x) = \sum_{i=0}^x (f_i - \langle f \rangle) \quad (27)$$

The average resulting fluctuations at each scale can then be statistically characterized across multiple moments, the standard method is to evaluate the  $q^{\text{th}}$  statistical moments. For  $q \leq 2$ , the generalized structure are defined, with  $q = 2$  corresponding to the classical case. We do not consider  $q > 2$  since the statistical moments may all depend on the largest value in the sample, spuriously leading to linear behavior in the exponent (and diverging as the sample size increases) [20]. To reuse what was previously explained in Section 2.1., the structure function function is now

$$S_{q(\Delta x)} = \langle |\mathcal{H}(\Delta x)|^q \rangle \sim \Delta x^{\xi(q)} \quad (28)$$

Note that planetary data usually contains radial and horizontal uncertainty which also needs to be accounted. This parts needs more discussion and precision, lets just define the dependence explicitly

$$\begin{aligned}\mathcal{H} &= Af(x) + Bf\left(x + \frac{\Delta x}{2}\right) + Cf(x + \Delta x) \\ A &= \frac{2}{\Delta x}, \quad B = -\frac{4}{\Delta x}, \quad C = \frac{2}{\Delta x}\end{aligned}\tag{29}$$

Propagation of the variance

$$\begin{aligned}\sigma_{\mathcal{H}}^2 &= (A^2 + B^2 + C^2)\sigma_r^2 \\ \sigma_{\mathcal{H}} &= \frac{\sigma_r \sqrt{24}}{\Delta x}\end{aligned}\tag{30}$$

However since Haar fluctuation values are not inferior to 1, and  $\min(\sigma_{\mathcal{H}}) = 0.0122$ , the radial uncertainty is clearly negligible. Actually for the Mars MOLA/HRSC dataset the  $\min(\sigma_{\mathcal{H}}) = 5.6e-7 \ll 1$ .

Now lets look at the horizontal uncertainties, supposed the measured point at horizontal  $\bar{x} = x + \delta x$  with  $\delta x$  a random variable with a standard deviation  $\sigma_h$ .

For the following results was used planetary data from Mars MOLA<sup>14</sup>, Mars MOLA/HRSC<sup>15</sup>, Mercury MLA USGS<sup>16</sup>, Mercury MLA from BepiColombo team, Moon LOLA<sup>17</sup>, Moon LOLA/SELENE<sup>18</sup>. The following Figure 19, Figure 20 and Figure 21 used the Mars MOLA/HRSC dataset, since it is at the moment the best DEM available for Mars and Mars being the most studied planets with the Haar wavelet method. All results are available in Section A.

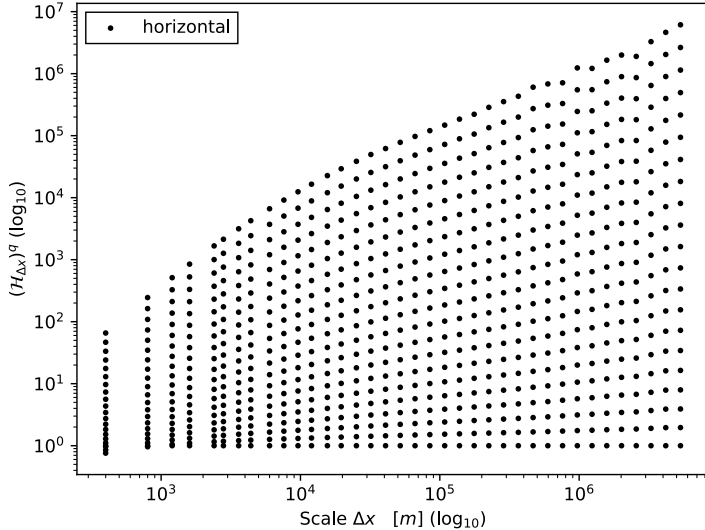


Figure 19: Haar horizontal fluctuations results for  $q \in [0, 2]$  at each scale  $\Delta x \in [2, \frac{L}{2}]$  from Mars MOLA HRSC 200m/pix dataset. In red are the pure horizontal mean fluctuations and in black its correction based on the altitude and row index, see Equation 31. The differences is greater at low scales meaning high latitudes are in fact important and play a crucial role in the overall surface statistic properties.

We now need to consider the case of high latitudes deformation caused by equicylindrical projection of planetary data representation. The objectif is to replace the classic pixel indexing by the real scale

<sup>14</sup>[https://astrogeology.usgs.gov/search/map/mars\\_mgs\\_mola\\_dem\\_463m](https://astrogeology.usgs.gov/search/map/mars_mgs_mola_dem_463m)

<sup>15</sup>[https://astrogeology.usgs.gov/search/map/mars\\_mgs\\_mola\\_mex\\_hrsc\\_blended\\_dem\\_global\\_200m](https://astrogeology.usgs.gov/search/map/mars_mgs_mola_mex_hrsc_blended_dem_global_200m)

<sup>16</sup>[https://astrogeology.usgs.gov/search/map/mercury\\_messenger\\_global\\_dem\\_665m](https://astrogeology.usgs.gov/search/map/mercury_messenger_global_dem_665m)

<sup>17</sup>[https://astrogeology.usgs.gov/search/map/moon\\_lro\\_lola\\_dem\\_118m](https://astrogeology.usgs.gov/search/map/moon_lro_lola_dem_118m)

<sup>18</sup>[https://astrogeology.usgs.gov/search/map/moon\\_lro\\_lola\\_selene\\_kaguya\\_tc\\_dem\\_merge\\_60n60s\\_59m](https://astrogeology.usgs.gov/search/map/moon_lro_lola_selene_kaguya_tc_dem_merge_60n60s_59m)

in meter and to keep scale homogeneity across latitudes. To do so, for each row we compute a  $\cos(\theta)$  correction:

$$\begin{aligned}\theta &= \pi \left( \frac{1}{2} - \frac{i}{n} \right) \\ \Delta\bar{x} &= \frac{\Delta x}{\cos(\theta)}\end{aligned}\tag{31}$$

Where  $i$  is the row number and  $n$  the total number of rows. Note that  $\Delta\bar{x}$  must also be paired and respect the  $\Delta x$  domain definition. We then use this new scale parameter in the algorithm loop and if the new scale calculated for a row is bigger than the overall row length, then we skip it.

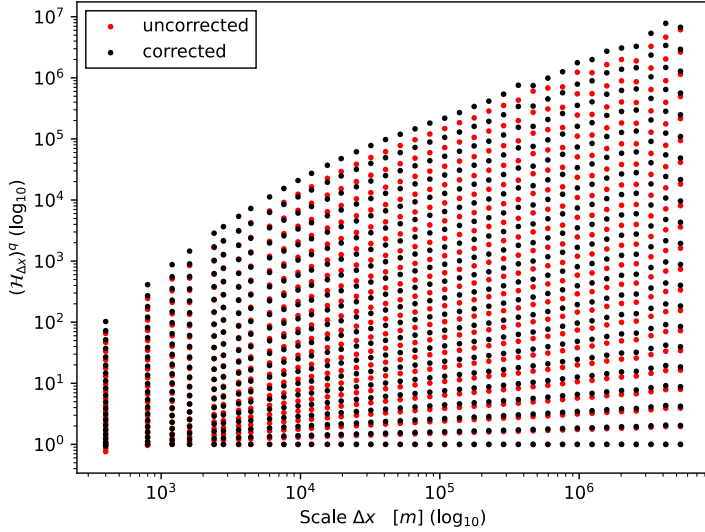


Figure 20: Haar horizontal fluctuations results for  $q \in [0, 2]$  at each scale  $\Delta x \in [2, \frac{L}{2}]$  from Mars MOLA HRSC 200m/pix dataset. In red are the pure horizontal mean fluctuations and in black its correction based on the altitude and row index, see Equation 31. The differences is greater at low scales meaning high latitudes are in fact important and play a crucial role in the overall surface statistic properties.

The final mean Haar evaluation across scales and directions needs to be equally consider through the horizontal and vertical. Since the data projection is equicylindrical, the total number of fluctuations per row  $n_{\Delta x}$  is bigger horizontally. Perhaps, we need to compute how many fluctuations are performed per row per scale to tackle this problem. The “weight” or number of fluctuations  $\omega$  is then used in the final result Equation 32.

$$\mathcal{H} = \langle \omega, \{\mathcal{H}_>, \mathcal{H}_\vee\} \rangle\tag{32}$$

Note that the  $>$  symbol represents the vertical direction from left to right and  $\vee$  the vertical direction from top to bottom. To perform the vertical fluctuation of a matrix array, we simply applied a transposed operation which rotate clockwise the data.

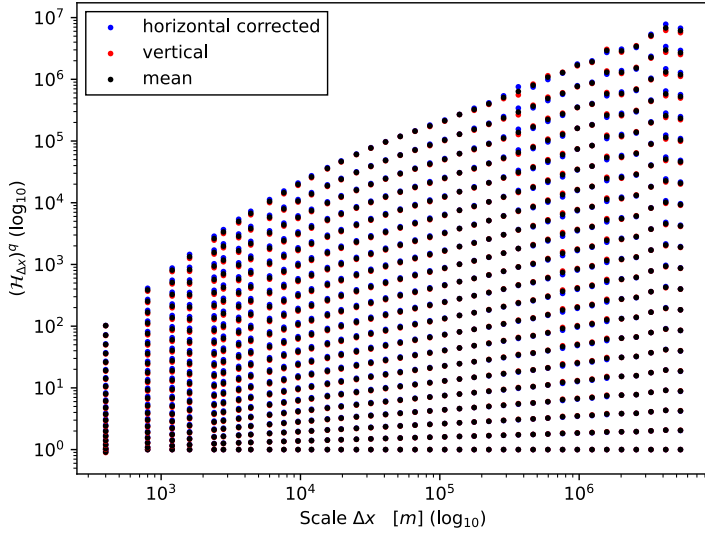


Figure 21: Haar fluctuations results for  $q \in [0, 2]$  at each scale  $\Delta x \in [2, \frac{L}{2}]$  from Mars MOLA HRSC 200m/pix dataset. In blue are the horizontal fluctuation corrected (see Figure 20), red the vertical fluctuations and black the weighted mean.

As expected, there is no significant differences between vertical and horizontal fluctuations, which confirms statistical isotropy [21]. Note that a small perturbation around 350 km occurs, which could be explained by local geological features like Valles Marineris.

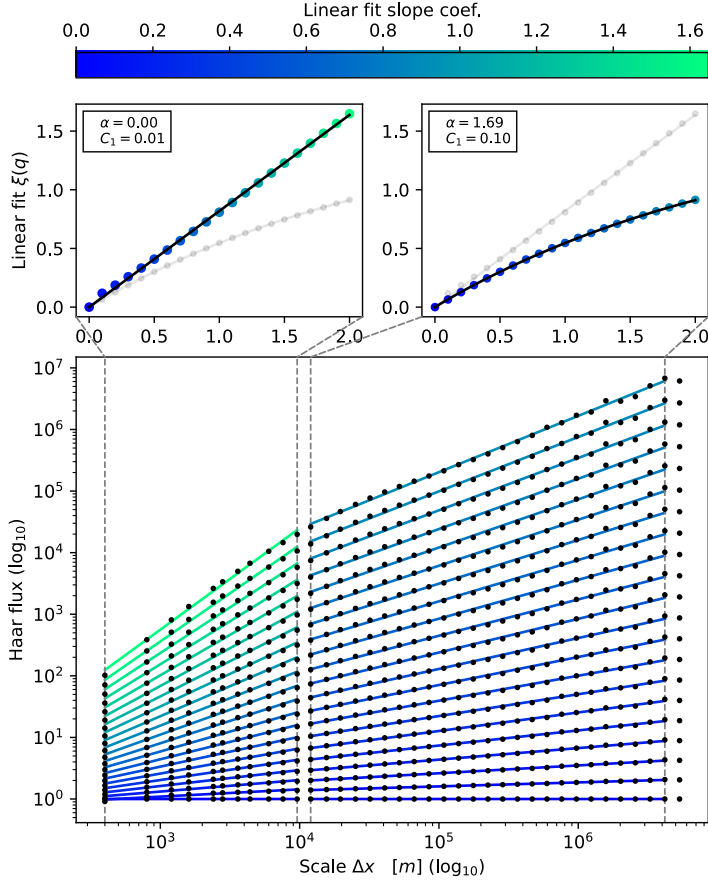


Figure 22: Haar fluctuations results for  $q \in [0, 2]$  at each scale  $\Delta x \in [2, \frac{L}{2}]$  from Mars MOLA HRSC 200m/pix dataset. Comparison between 2 regimes, monofractal  $< 10$  km and multifractal  $> 10$  km The gradient color corresponds to the linear fit slope coefficient.

The Figure 22 shows very interesting results where 2 regimes are clearly identified, the first one below 10 km is monofractal and above is multifractal. These regimes are very distinct with a net transition chosen experimentally. From Equation 23 we retrieved for each regime the fitted parameters  $\alpha$ ,  $C_1$  and  $H$  which emphasize our suggested 2 regimes behaviour. Note that for  $C_1 < 2e-3$  we consider monofractality.

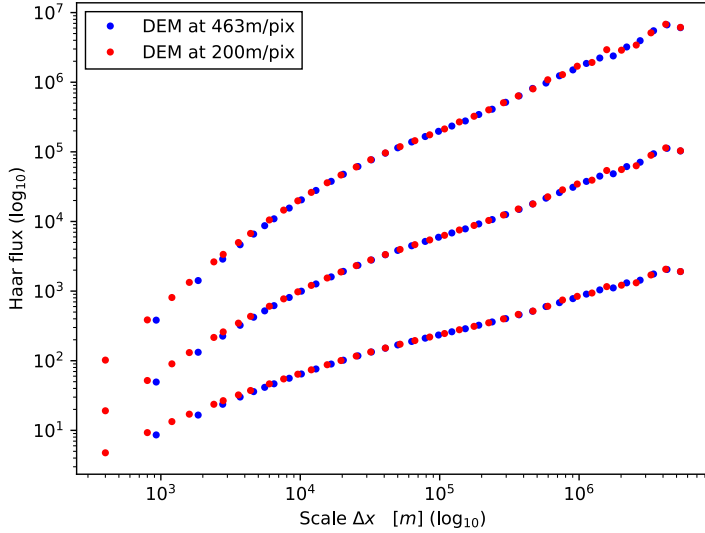


Figure 23: Haar fluctuations results for  $q \in [0, 2]$  at each scale  $\Delta x \in [2, \frac{L}{2}]$  from Mars MGS+HRSC DEM at 200m/pix in red and MGS DEM at 463m/pix in red. Comparison between two haar fluctuation results over the entire DEM of Mars for different resolution

From this comparison we can ensure the conservation of statistical properties within the new enhanced resolution DEM HRSC+MGS. At high scales the values are conserved and at low scales they are slightly higher which is exactly what we were expecting, since the new detailed DEM increase the overall mean height differences. This demonstrates a great tool to analyze and verify upscaling methods. However, we also applied the same study on many different dataset and results needs to be more carefully detailed.

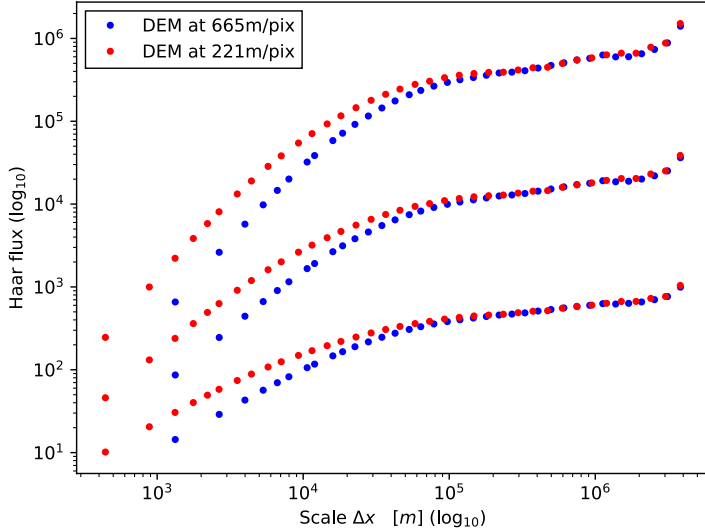


Figure 24: Haar fluctuations results for  $q \in [0, 2]$  at each scale  $\Delta x \in [2, \frac{L}{2}]$  from Mercury Messenger DEM from Preusker at 200m/pix in red and Messenger DEM from Becker at 665m/pix in blue. Comparison between two haar fluctuation results over the entire DEM of Mars for different resolution

Clear exemple of what we should more detailed what is hapening !!

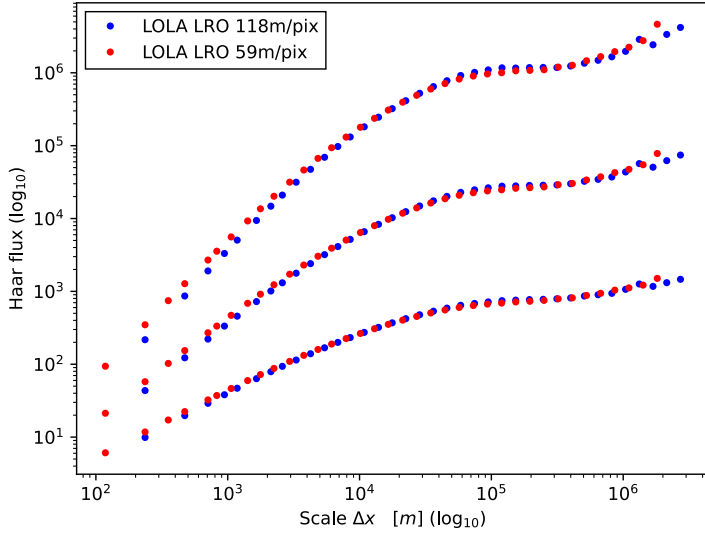


Figure 25: Haar fluctuations results for  $q \in [0, 2]$  at each scale  $\Delta x \in [2, \frac{L}{2}]$  from Mars MGS+HRSC DEM at 200m/pix and MGS DEM at 463m/pix datasets. Comparison between two haar fluctuation results over the entire DEM of Mars for different resolution

## 2.3. Multifractal generator

Several probability distributions can serve as potential candidates for modeling random fields. Among them, the Gaussian distribution is by far the most commonly employed in the literature, owing to its mathematical simplicity and its deep connection with the central limit theorem. The Gaussian assumption is often motivated by the underlying physics of the problem and, in many cases, allows for analytical or closed-form solutions. However, when the field exhibits strong intermittency or heavy-tailed behavior, Gaussian statistics become inadequate.

A class of distribution that generalizes the Gaussian while accounting for heavier tails is the Lévy  $\alpha$ -stable family. Multifractal fields, in particular, with often pronounced intermittency and extreme fluctuations. Those characteristics are common in planetology, especially in planetary topographies such as the Valles Marineris on Mars. To realistically generate synthetic topographies with multifractal structures, an  $\alpha$ -stable distribution with power-law tails provides a more accurate representation of these rare and large deviations that Gaussian models fail to capture.

At the core of additive multifractal cascade models lies the requirements for an  $\alpha$ -stable distribution. Indeed, propagating and conserving coherent statistical properties through successive cascade levels (the so-called  $\alpha$ -model) necessitates the use of independent, identically distributed, heavy tailed random variables that exhibit sum-stability. This property ensures that the statistical form of the distribution remains invariant under aggregation, thereby preserving the self-similar structure of the multifractal field across scales.

### 2.3.1. Stable random variables generator

In probability theory, a distribution is called stable if a linear combination of two independent random variables has in result the same distribution. The stable distribution family, also called the Lévy  $\alpha$ -stable distribution can easily be constructed with a numerical method (see Weron 1991 [22] for full proof) :

$$\begin{aligned}
X &= S_{\alpha,\beta} \frac{\sin(\alpha(V + B_{\alpha,\beta}))}{\cos(V)^{\frac{1}{\alpha}}} \left( \frac{\cos(V - \alpha(V + B_{\alpha,\beta}))}{W} \right)^{\frac{1-\alpha}{\alpha}} \\
B_{\alpha,\beta} &= \frac{\arctan(B \tan(\frac{\pi\alpha}{2}))}{1 - |1 - \alpha|} \\
S_{\alpha,\beta} &= \left( 1 + \left( -\beta \tan\left(\frac{\pi\alpha}{2}\right) \right)^2 \right)^{\frac{1}{2\alpha}}
\end{aligned} \tag{33}$$

Note that this methods is valid for  $\alpha \in ]0, 2]$  and  $\alpha \neq 1$  and  $\beta \in [-1, 1]$ . Generate a random variable  $V$  uniformly distributed on  $(-\frac{\pi}{2}, \frac{\pi}{2})$  and an independent exponential random variable  $W$  with mean  $\lambda = 1$ .

### 2.3.2. FIF generator

$$\Gamma_\lambda(x) = C_1^{\frac{1}{\alpha}} \int_{\mathbb{R}^D} \frac{\lambda_0^\alpha(dx')}{|x - x'|^{D-H}} - \text{var}(\alpha) \log(\lambda), \quad \text{var}(\alpha) = \frac{C_1}{\alpha - 1} \tag{34}$$

$$\int_{\mathbb{R}^D} \frac{\lambda_0^\alpha(dx')}{|x - x'|^{D-H}} \approx \sum^i \frac{X_i(\Delta x^D)}{|x - x_i|^{D-H}} \tag{35}$$

## 2.4. Synthetic topography modeling

Synthetic topography is found in many distinct study fields, from games, agriculture up to AI image generation. At the core of generating synthetic topography lies the fundamental use of random distribution. These distributions represents the underlying physics for different geological terrain particularity (crater, canyon, plains, mountains, etc.) and can be categorized by 2 main fractal regime as described in Table 9. The monofractal, which is the repetition of the same pattern at each scale and the multifractal, which is a repetition of a pattern evolving across different scales.

<b>Model</b>	<b>Field</b>	<b>Fractal law</b>
Monofractal fLM	$H' = H + \frac{d}{\alpha}$ $v(\underline{r}) = \gamma_\alpha *  \underline{r} ^{-(d-H')}$	$\xi(q) = \begin{cases} qH, & q < \alpha \\ \infty, & q > \alpha \end{cases}$
Multifractal FIF	$H_{\alpha'} = \frac{d}{\alpha'} \quad   \quad \alpha' = \frac{\alpha}{\alpha-1}$ $\Gamma \propto C_1^{\frac{1}{\alpha'}} \gamma_\alpha *  \underline{r} ^{-(d-H_{\alpha'})}$ $v(\underline{r}) = e^\Gamma *  \underline{r} ^{-(d-H)}$	$\xi(q) = qH - K(q)$

Table 9: A comparison of various scaling models for  $v$  showing the essential similarities and differences in their mathematical structure, fractal power law. The  $\gamma_\alpha$  term is described by the CMS<sup>19</sup> method,  $\xi(q)$  a linear structure function exponent of the field fractality

To avoid huge numerical time computing, we used the frequency domain and transformed the multifractal generation model kernel in:

$$|\underline{r}|^{-(d-H)} \xrightarrow{\text{F.T.}} |\underline{k}|^{-H} \tag{36}$$

---

<sup>19</sup>Chambers Mallows Stuck

### 2.4.1. Deconvolution using Levy generator method

In this part we tackle the upscaling of a digital elevation model, through the height statistical conservation of a field. We simply started with a code to generate synthetic topography Figure 28 using levy-alpha stable distribution see Figure 26 and then a tool that downscale the initial generated field. Then inverse the  $e^\Gamma$  value Figure 27 and add n cascade [11] to it to mimic what could have been lower scale noise. Finally we regenerate the topography. The full pipeline is described here

$$v(\underline{r}) * |\underline{r}|^{(d-H)} = e^\Gamma$$

$\log(v(\underline{r}) * |\underline{r}|^{(d-H)}) \times C_1^{-\frac{1}{\alpha}} * |\underline{r}|^{(d-H_{\alpha'})} = \Gamma$

(37)

*Algo (s, n):*

```

1  $n = 2^k, k \in \mathbb{Z}_{\geq 0}$ 
2  $e^\Gamma = s * |\underline{r}|^{(d-H)}$ 
3 for  $k \leftarrow 1$  to  $\log_2(n)$ :
4    $e_k^\Gamma = e_{k-1}^\Gamma \otimes 1^{(2 \times 2)}, e_{k-1}^\Gamma \in \mathbb{R}^{(m \times n)}$ 
5    $\psi = 2^{(\frac{d}{\alpha} - d)}$ 
6   for  $i \leftarrow 0$  to  $m$  by 2:
7     for  $j \leftarrow 0$  to  $n$  by 2:
8        $\hat{e}_{ij}^\Gamma = C_1^{-\frac{1}{\alpha}} \gamma_\lambda * |\underline{r}|^{(d-H_{\alpha'})} \times \psi, \gamma_\lambda \in \mathbb{R}^{(2 \times 2)}$ 
9        $\hat{e}_{ij}^\Gamma = \frac{\hat{e}_{ij}^\Gamma}{\langle \hat{e}_{ij}^\Gamma \rangle}$ 
10       $e_k^\Gamma \{^{[i:i+2]}_{[j:j+2]} = \hat{e}_{ij}^\Gamma \cdot e_k^\Gamma \{^{[i:i+2]}_{[j:j+2]}$ 

```

To verify the validity of our model we implemented 2 new pipeline. The first one validate the self loop of the deconvolution for an upscale set to 1. We start from a synthetic fractal field created from the classic method using Fourier convolution, and we inverse it back to see if we retrieve the initial noise used to initialize the synthetic fractal field. When this loop is verified, next the homogeneity in the global pipeline needs to be checked. For that, we simply start again from a synthetic fractal field created from the classic method using Fourier convolution, then downscaled  $n$  times. This “blured” new fractal field act as the image retrieved in real life, which needs to be upscaled. We took this downscaled fractal field and inversed it only for the first convolution Table 9, resulting in  $e^\Gamma$ , we will call it “alpha noise”. From this alpha noise, can be added new cascade (we avoid recomputing the convolution in Fourier)  $n$  times, resulting in a statistical similar fractfield, with new small scale features but with respect to the field nature.

This approach uses a discret numerical reconstruction (adding cascade) to a continuous cascade made fractal field. However, a problem occurs, due to the generation of small 2x2 noise to construct the next scale cascade. We see a discontinuity between each new 2x2, it feels like the overall  $n + 1$  cascade doesn't have a global behaviour link. While, if we generate the noise for the  $n + 1$  cascade of size  $\text{dim}^*2$ , we obtain way more smooth results, with coherent global behaviour.

$$\begin{aligned} \mathcal{P}(\mu_\varepsilon = \lambda^{\gamma_+}) &= \lambda^{-c} \\ \mathcal{P}(\mu_\varepsilon = \lambda^{\gamma_-}) &= 1 - \lambda^{-c} \end{aligned} \quad (38)$$

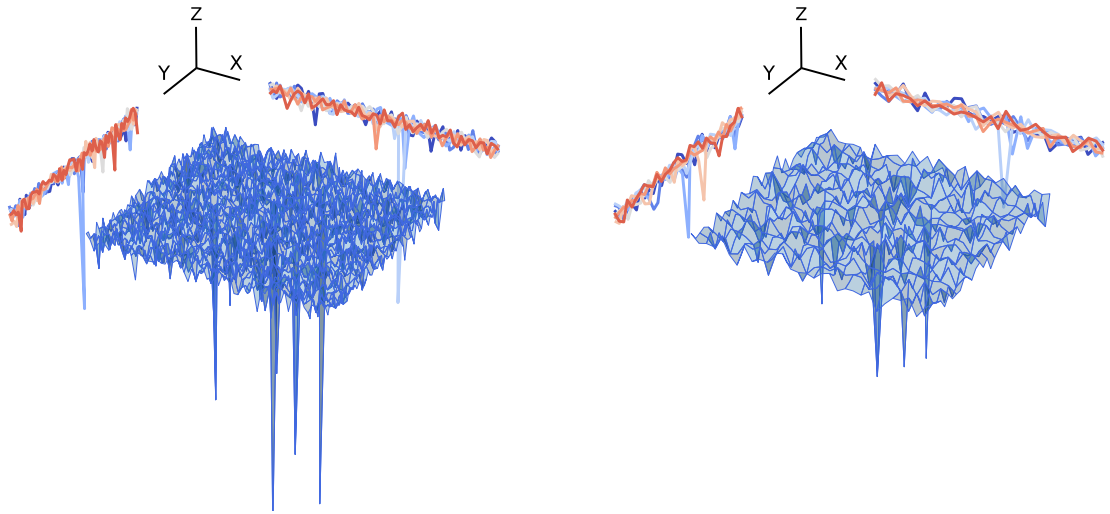


Figure 26: BLABLABLA

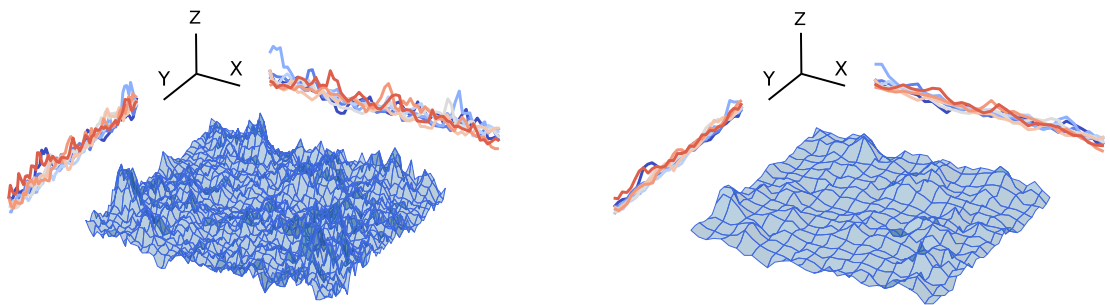


Figure 27: BLABLABLA

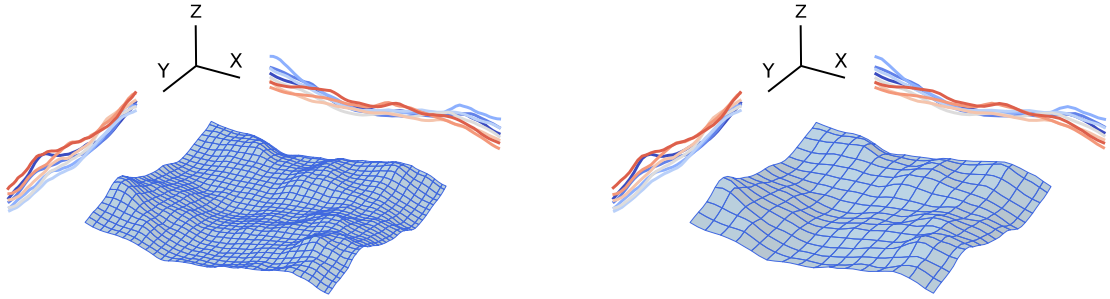


Figure 28: BLABLABLA

#### 2.4.2. Fourier filtering

We discovered that by generating cascade to enhance the resolution, appears squared artefact. This affect the result, especially for high scale variation when we reconstruct the upscaled field. First intuition is to use a Fourier filter that remove border frequency.

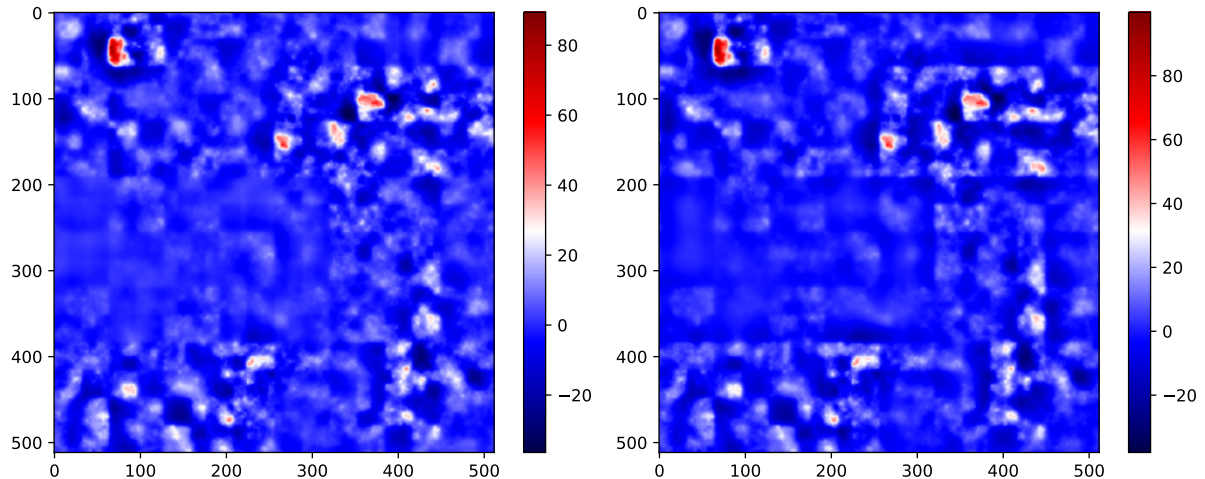


Figure 29: BLABLABLA

To distinguish the added topography from the cascade method, we implemendted a Fourier filter which seperates the new frequencies corresponding to small scales smaller than the upscaling coefficient and high scales, the rest.

$$G(\omega) = \frac{1}{\sqrt{1 + \omega^{2n}}} \quad (39)$$

### 2.4.3. Formation UQ ed SMEMAG

#### Day 1:

Theory (Hapke) → Exp. (Photo-gonio meter) → Model (BRDF) → Num. (MC Inversion) → Pred.

- [Num.] Uncertainties propagation (Many measurements)

Note: known and unknown uncertainty

- [Model] Modeling of uncertainties (Local measurement)

- [Pred.] Decision under uncertainty (Accept, reject or create uncertainties model)

Note: needs of a robust control or optimization and a sensitivity analysis

**Slide 1-4:** VVUQ required for Haar fluctuation and MCMC Inversion

**Slide 1-8:**  $\xi$  is the x-absiss,  $\mathcal{P}(\xi)$  the green distribution,  $X$  the red line and  $\mathcal{P}(X)$  the output distribution y-ordo.

**Slide 2-2:** Theorem central lim says that N times the average tends to the true mean and the proba tends to the normal gaussian distribution

**Slide 2-11:** Symetrization of Integrand, symetrization of only the parameter we want  $X(\xi) = X(\xi_1, \dots, \xi_N)$  which can be decomposed in  $G(\xi_1) + F(\xi_1, \dots, \xi_N)$  for  $\xi_1$  being the dominant weight parameter

**Slide 2-2:** We can inverse the distribution and get back through the  $CDF^{-1}$  the original law (and parameters ?)

**Slide 3-6** histograms kernel appro for true density

#### Day 2:

**MCMC** method:

$$\{\xi^{(i)}, \quad i = 1, \dots, N\}$$

transition probability  $\rightarrow P_T(\xi^{(i+1)} | \xi^{(i)})$

such that  $\lim_{i \rightarrow \infty} \xi^{(i)} \sim \mathcal{P}_\xi$

Drawing random samples from multivariate Gaussian distribution.

$N(\mu, \Sigma^2)$ ,  $\mu \in \mathbb{R}^d$ ,  $\Sigma^2 \in \mathbb{R}^{d \times d}$ , symmetric positive matrix.

$$\xi = \begin{pmatrix} \xi_1 \\ \xi_2 \\ \vdots \\ \xi_d \end{pmatrix} \sim N(\mu, \Sigma^2) \text{ and } \Sigma_{ij}^2 = \mathbb{E}[\xi_i \xi_j] - \mu_i \mu_j$$

We have a random number generator to draw  $\eta \sim N(0, 1)$

Cholesky decomposition (not robust if low values on the diag):

$$\Sigma^2 = LL^T \rightarrow \begin{pmatrix} \xi_1 \\ \vdots \\ \xi_d \end{pmatrix} (\omega), \quad \mathbb{E}((\xi - \mu)(\xi - \mu)^T) = LL^T$$

Eigen decomposition:

$$\Sigma^2 = U \Lambda U^T, \quad U \text{ is unity}, \quad \Lambda = \text{diag}(\lambda_i)$$

#### Day 3:

Data / parameters uncertain

$$D(\Theta) \in \mathcal{P}(\theta, \xi(\theta), \mu(\theta))$$

Model (deterministic)

$$\mathcal{M}(u(\theta), D(\theta)) = 0$$

Quantity of interested

$$\Phi(u(\theta)) \in \mathcal{P}$$

Polynomial Chaos expansions (Wioner 1938, Cameron and Martin 1947, Charum and spanos 1991)

Wiener:  $a(\theta)$  a random quantity that behaves reasonably, then

$$a(\theta) = \lim_{N \rightarrow \infty} a_0 \Gamma_0 + \sum_{i_1=0}^N a_{i_1} \Gamma_1(\xi_{i_1}(\theta)) + \sum_{i_1=0}^N \sum_{i_2=i_1}^N a_{i_2} \Gamma_2(\xi_{i_1}(\theta), \xi_{i_2}(\theta)) + \dots \quad (40)$$

$\Gamma_i$  represent a polynomial of degree  $i$  and  $\xi_1, \dots, \xi_N$  are iid standard gaussian RV.

Uncertainty germ  $\xi_1, \dots, \xi_N \rightarrow$  transformed by polynomial to get approximate the initial random variable.

GPC pour retrouver la distribution d'un field multifractal avec une combinaison de plusieurs différentes distributions qui aurait ou non des inputs indépendants. Méthode 1: stochastic galerkin projection (conacter olivier si des questions)

Méthode 2: Non intrusive

# 3

## Background

### 3.1. What is Typst?

Typst is a modern markup-based typesetting system designed to be a powerful yet user-friendly alternative to LaTeX. Released in 2023, it combines the simplicity of Markdown with the typographic quality and programmability traditionally associated with LaTeX, making it an excellent choice for academic writing.

Key advantages of Typst include:

- **Fast compilation:** Near-instantaneous preview updates as you type
- **Clear error messages:** Helpful diagnostics that pinpoint exactly what went wrong
- **Modern syntax:** Intuitive markup that's easier to learn than LaTeX
- **Built-in scripting:** Powerful programming capabilities for advanced customization
- **Excellent math support:** Beautiful mathematical typesetting out of the box

### 3.2. Why a Typst Template?

While LaTeX has been the de facto standard for academic typesetting for decades, its steep learning curve and cryptic error messages can be cumbersome. This Typst template maintains compatibility with University of Basel's formatting requirements while offering a more approachable writing experience.

The template handles all the formatting details automatically, allowing you to focus on your content rather than wrestling with compilation errors or obscure package conflicts.

# 4

## Discussion

Use the `\orem()` command to add some meaningful text quickly.

  Lorem ipsum dolor sit amet, consectetur adipiscing elit, sed do eiusmod tempor incididunt ut labore et dolore magna aliquam quaerat voluptatem. Ut enim aequo doleamus animo, cum corpore dolemus, fieri tamen permagna accessio potest, si aliquod aeternum et infinitum impendere malum nobis opinemur. Quod idem licet transferre in voluptatem, ut postea variari voluptas distingue possit, augeri amplificarique non possit. At etiam Athenis, ut e patre audiebam facete et urbane Stoicos irridente, statua est in quo a nobis philosophia defensa et collaudata est, cum id, quod maxime placeat, facere possimus, omnis voluptas assumenda est, omnis dolor repellendus. Temporibus autem quibusdam et aut officiis debitibus aut rerum necessitatibus saepe eveniet, ut et voluptates repudiandae sint et molestiae non recusandae. Itaque earum rerum defuturum, quas natura non depravata desiderat. Et quem ad me accedis, saluto: 'chaere,' inquam, 'Tite!' lictores, turma omnis chorusque: 'chaere, Tite!' hinc hostis mi Albucius, hinc inimicus. Sed iure Mucius. Ego autem mirari satis non queo unde hoc sit tam insolens domesticarum rerum fastidium. Non est omnino hic docendi locus; sed ita prorsus existimo, neque eum Torquatum, qui hoc primus cognomen invenerit, aut torquem illum hosti detraxisse, ut aliquam ex eo est consecutus? – Laudem et caritatem, quae sunt vitae sine metu degendae praesidia firmissima. – Filium morte multavit. – Si sine causa, nollem me ab eo delectari, quod ista Platonis, Aristoteli, Theophrasti orationis ornamenta neglexerit. Nam illud quidem physici, credere aliquid esse minimum, quod profecto numquam putavisset, si a Polyaeno, familiari suo, geometrica discere maluisset quam illum etiam ipsum dedocere. Sol Democrito magnus videtur, quippe homini erudo in geometriaque perfecto, huic pedalis fortasse; tantum enim esse omnino in nostris poetis aut inertissimae segnitiae est aut fastidii delicatissimi. Mihi quidem videtur, inermis ac nudus est. Tollit definitiones, nihil de dividendo ac partiendo docet, non quo ignorare vos arbitrer, sed ut.

# 5

## Conclusion

This tutorial has demonstrated that Typst provides a viable, modern alternative to LaTeX for academic thesis writing.

By adopting Typst, you can focus on your research and writing rather than fighting with compilation errors. I hope this template helps make thesis writing a more pleasant and productive experience.

# Bibliography

- [1] C. D. Murray and S. F. Dermott, *Solar system dynamics*. Cambridge [u.a]: Cambridge Univ. Press, 2012. doi: 10.1017/CBO9781139174817.
- [2] M. A. Wieczorek, “The Constitution and Structure of the Lunar Interior,” *Reviews in Mineralogy and Geochemistry*, vol. 60, no. 1, pp. 221–364, Jan. 2006, doi: 10.2138/rmg.2006.60.3.
- [3] B. Hapke, *Theory of Reflectance and Emittance Spectroscopy*. Cambridge: Cambridge University Press, 2012. doi: <https://doi.org/10.1017/CBO9781139025683>.
- [4] B. L. Jolliff, J. J. Gillis, L. A. Haskin, R. L. Korotev, and M. A. Wieczorek, “Major lunar crustal terranes: Surface expressions and crust-mantle origins,” *Journal of Geophysical Research: Planets*, vol. 105, no. E2, pp. 4197–4216, 2000, doi: 10.1029/1999JE001103.
- [5] F. Schmidt and S. Bourguignon, “Efficiency of BRDF sampling and bias on the average photometric behavior,” *Icarus*, vol. 317, pp. 10–26, Jan. 2019, doi: 10.1016/j.icarus.2018.06.025.
- [6] S. Chandrasekhar, *Radiative Transfer*. Courier Corporation, 1960.
- [7] A. F. McGuire and B. W. Hapke, “An Experimental Study of Light Scattering by Large, Irregular Particles,” *Icarus*, vol. 113, no. 1, pp. 134–155, Jan. 1995, doi: 10.1006/icar.1995.1012.
- [8] A. L. Souchon *et al.*, “An experimental study of Hapke’s modeling of natural granular surface samples,” *Icarus*, vol. 215, no. 1, pp. 313–331, Sept. 2011, doi: 10.1016/j.icarus.2011.06.023.
- [9] H. Sato, M. S. Robinson, B. Hapke, B. W. Denevi, and A. K. Boyd, “Resolved Hapke parameter maps of the Moon,” *Journal of Geophysical Research: Planets*, vol. 119, no. 8, pp. 1775–1805, 2014, doi: 10.1002/2013JE004580.
- [10] P. Cubillos, J. Harrington, T. J. Loredo, N. B. Lust, J. Blecic, and M. Stemm, “On correlated-noise analyses applied to exoplanet light curves,” *The Astronomical Journal*, vol. 153, no. 1, p. 3, Jan. 2017, doi: 10.3847/1538-3881/153/1/3.
- [11] S. Lovejoy and D. Schertzer, *The Weather and Climate: Emergent Laws and Multifractal Cascades*. Cambridge: Cambridge University Press, 2013. doi: 10.1017/CBO9781139093811.
- [12] A. N. Kolmogorov, “The Local Structure of Turbulence in Incompressible Viscous Fluid for Very Large Reynolds Numbers,” *Proceedings: Mathematical and Physical Sciences*, vol. 434, no. 1890, pp. 9–13, 1991, [Online]. Available: <http://www.jstor.org/stable/51980>
- [13] U. Frisch, P.-L. Sulem, and M. Nelkin, “A simple dynamical model of intermittent fully developed turbulence,” *Journal of Fluid Mechanics*, vol. 87, no. 4, pp. 719–736, Aug. 1978, doi: 10.1017/S0022112078001846.
- [14] S. Lovejoy and D. Schertzer, “Haar wavelets, fluctuations and structure functions: convenient choices for geophysics,” *Nonlinear Processes in Geophysics*, vol. 19, no. 5, pp. 513–527, Sept. 2012, doi: 10.5194/npg-19-513-2012.
- [15] F. Landais, F. Schmidt, and S. Lovejoy, “Multifractal topography of several planetary bodies in the solar system,” *Icarus*, vol. 319, pp. 14–20, Feb. 2019, doi: 10.1016/j.icarus.2018.07.005.
- [16] E. Foufoula-Georgiou and P. Kumar, *Wavelet Analysis in Geophysics*, vol. 4. in Wavelets in Geophysics, vol. 4. Academic Press, 1994. doi: 10.1016/B978-0-08-052087-2.50007-4.

- [17] C. Torrence and G. P. Compo, “A Practical Guide to Wavelet Analysis,” *Bulletin of the American Meteorological Society*, vol. 79, no. 1, pp. 61–78, Jan. 1998, doi: 10.1175/1520-0477(1998)079<0061:APGTWA>2.0.CO;2.
- [18] A. Haar, “Zur Theorie der orthogonalen Funktionensysteme,” *Mathematische Annalen*, vol. 69, no. 3, pp. 331–371, Sept. 1910, doi: 10.1007/BF01456326.
- [19] A. Sanner, W. G. Nöhring, L. A. Thimons, T. D. B. Jacobs, and L. Pastewka, “Scale-dependent roughness parameters for topography analysis,” *Applied Surface Science Advances*, vol. 7, p. 100190, Feb. 2022, doi: 10.1016/j.apsadv.2021.100190.
- [20] J.-S. Gagnon, S. Lovejoy, and D. Schertzer, “Multifractal earth topography,” *Nonlinear Processes in Geophysics*, vol. 13, no. 5, pp. 541–570, Oct. 2006, doi: 10.5194/npg-13-541-2006.
- [21] F. Landais, F. Schmidt, and S. Lovejoy, “Universal multifractal Martian topography,” *Nonlinear Processes in Geophysics*, vol. 22, no. 6, pp. 713–722, Nov. 2015, doi: 10.5194/npg-22-713-2015.
- [22] R. Weron, “On the Chambers-Mallows-Stuck method for simulating skewed stable random variables,” *Statistics & Probability Letters*, vol. 28, no. 2, pp. 165–171, June 1996, doi: 10.1016/0167-7152(95)00113-1.

# A

## Appendix

Proxy results for every geometry at $\varepsilon = 10\%$						
n° orbit	E		M		H	
	$\sigma = 10\%$	$\sigma = 2\%$	$\sigma = 10\%$	$\sigma = 2\%$	$\sigma = 10\%$	$\sigma = 2\%$
1	5.2652	4.1852	3.7664	2.6399	4.2671	1.7961
2	3.5817	2.5636	3.6171	1.0457	3.8480	0.9529
3	4.6380	3.7279	3.3332	1.8276	3.7549	1.5833
4	4.5780	3.6650	1.7607	1.2815	3.8267	0.5242
5	5.6045	5.4796	4.0150	3.1180	4.7915	1.3229
12	2.1425	0.7131	1.3266	0.1607	1.7009	0.0979
13	3.5545	1.3644	2.2468	0.4984	2.8786	0.3233
14	2.4700	1.0576	0.8783	0.3285	2.1917	0.1324
15	3.9741	2.3920	1.6099	0.4009	2.3919	0.2830
23	1.7769	0.4467	2.0091	0.1722	1.8882	0.1151
24	2.1002	0.7535	0.6372	0.1000	1.7221	0.0119
25	2.2511	1.1397	1.9620	0.1886	1.8312	0.1690
34	3.2573	1.3876	0.7060	0.2129	2.0803	0.0181
35	4.4379	3.0202	1.6961	0.3845	2.6798	0.2334
45	4.4263	2.9738	0.9161	0.7401	3.1343	0.0707
123	0.8717	0.1129	0.9863	0.1055	1.1176	0.0589
124	0.7900	0.1121	0.4137	0.0385	1.0113	0.0009
125	0.7993	0.1378	1.0494	0.0934	1.0876	0.0808
134	1.9215	0.5175	0.5397	0.2360	1.3388	0.0048
135	3.2652	1.0120	1.0816	0.1584	1.8373	0.0865
145	2.3642	0.9379	0.5371	0.1755	1.6543	0.0032
234	1.4727	0.3438	0.4247	0.0616	1.1461	0.0028
235	1.5098	0.3914	1.3000	0.1141	1.3632	0.0790
245	2.0076	0.6484	0.4946	0.0796	1.3823	0.0042
345	3.1085	1.1599	0.4894	0.1810	1.8117	0.0038
1234	0.6738	0.0876	0.3089	0.0261	0.7207	0.0003
1235	0.6717	0.1037	0.8209	0.0818	0.8820	0.0557
1245	0.7121	0.1089	0.3444	0.0315	0.8041	0.0008
1345	1.8730	0.5031	0.3849	0.0935	1.2480	0.0006
2345	1.3977	0.3159	0.3495	0.0483	1.0158	0.0015
12345	0.6079	0.0852	0.2667	0.0256	0.6623	0.0003

Table 10: Proxy results for every geometry combinations over all photometry with an acceptable range set to  $\varepsilon = 10\%$